



***Facultad de Ciencias***

**Electromagnetic behavior of plasmonic  
devices with nanoholes. Biosensing  
applications**  
(Comportamiento electromagnético de  
dispositivos plasmónicos con nanoagujeros.  
Aplicaciones en biosensores)

Trabajo de Fin de Máster  
para acceder al

**MÁSTER EN FÍSICA, INSTRUMENTACIÓN Y MEDIO  
AMBIENTE**

Autor: Ángela Barreda Gómez

Director/es: Fernando Moreno Gracia

Francisco González Fernández

Julio- 2014

## **Agradecimientos**

A los directores del trabajo por todo el apoyo y el esfuerzo realizado

A mi familia

# Index

<b>1. Introduction.....</b>	<b><u>2</u></b>
<b>1.1 Plasmonics.....</b>	<b><u>2</u></b>
<b>1.2 Surface plasmons.....</b>	<b><u>3</u></b>
<b>1.2.1 Different configurations for exciting surface plasmons.....</b>	<b><u>6</u></b>
<b>2. Objectives and work scheme.....</b>	<b><u>11</u></b>
<b>2.1 Objectives.....</b>	<b><u>11</u></b>
<b>2.2 Work scheme.....</b>	<b><u>11</u></b>
<b>3. Diffraction theory.....</b>	<b><u>13</u></b>
<b>4. Extraordinary Optical Transmission.....</b>	<b><u>16</u></b>
<b>4.1 Basics on Extraordinary Optical Transmission.....</b>	<b><u>16</u></b>
<b>4.2 Role of materials in EOT.....</b>	<b><u>18</u></b>
<b>4.3 Role of nanohole shape in EOT.....</b>	<b><u>20</u></b>
<b>4.4 Different nanostructures.....</b>	<b><u>22</u></b>
<b>5. Fabry-Perot resonances.....</b>	<b><u>24</u></b>
<b>6. Wood's anomalies.....</b>	<b><u>26</u></b>
<b>7. Effective medium theory.....</b>	<b><u>28</u></b>
<b>8. Numerical methods.....</b>	<b><u>29</u></b>
<b>9. Applications.....</b>	<b><u>30</u></b>
<b>9.1 Medicine and biology.....</b>	<b><u>30</u></b>
<b>9.2 Surface-Enhanced Raman Scattering.....</b>	<b><u>30</u></b>
<b>9.3 Another interesting applications.....</b>	<b><u>30</u></b>
<b>10. Results.....</b>	<b><u>31</u></b>
<b>10.1 Validation of effective medium theory.....</b>	<b><u>31</u></b>
<b>10.2 Sensitivity in different geometries.....</b>	<b><u>36</u></b>
<b>10.2.1 Basic device. Thin film with nanoholes.....</b>	<b><u>36</u></b>
<b>10.2.2 Thin film with nanoholes and cavity effects I .....</b>	<b><u>39</u></b>
<b>10.2.3 Thin film with nanoholes and cavity effects II.....</b>	<b><u>41</u></b>
<b>11. Conclusions &amp; future work.....</b>	<b><u>47</u></b>
<b>Bibliography.....</b>	<b><u>49</u></b>

## 1.1 Plasmonics

Interaction of electromagnetic radiation with matter to nanometric scale has opened a new research field in physics, providing results in different scientific areas as optics, materials, medicine...Quick technological development, experienced in the last decades, has allowed manufacturing nanostructured metallic systems. In this way, many theoretical results have been put in evidence through different experiments. The branch of physics devoted to the study of these items is nanophotonics.

In presence of electromagnetic radiation, gas of free electrons that constitute a metal oscillates at the same frequency as the incident radiation, generating plasmons. It is distinguished between two kind of plasmons: localized surface plasmons and surface plasmons (section 1.2). The second kind are responsible for the physical phenomena that will be studied during this work.

Diffraction suffered by light when it interacts with objects, has been a vastly studied field in optics. The theory published by Hans Bethe in 1944, established that normalized to the transmission area of light through a circular hole, which was perforated in an infinitely thin perfect conductor film, was directly (inversely) related to the fourth power of radius (wavelength of incident light) [1]. This means that the amount of light transmitted by the hole was really low. However, experimentally, in transmission spectra, clear peaks were observed, corresponding to some specific wavelengths where transmission of light after going through a periodic array of subwavelength apertures, perforated in a thin metal film, was considerably greater than the predicted by Bethe. This phenomenon, known as Extraordinary Optical Transmission (EOT), is due to the interaction between surface plasmon polaritons (SPP) modes formed in each one of the surfaces of the corrugated thin film [2].

From the EOT discovery, its use has been proposed for many different applications [3], some of the most important ones are: biosensors, subwavelength lithography, Surface Enhanced Raman Spectroscopy...

With the objective of getting higher sensitivities in biosensors, different nanostructures have been proposed. Some of the most usual variations consist on changing period, shape of apertures or metal which thin film is made of.

In this project, we have tried to advance in the knowledge of new nanostructured systems which provide high sensitivity and can be manufactured in an easy way with the current technology. We have investigated, using the Finite Element Method (FEM), the EOT phenomenon through holes perforated in gold thin films, deposited on a dielectric substrate. We have obtained reflection and transmission spectra for different geometries and configurations and calculated sensitivity of the designed device to changes in the refractive index of a medium. Particularly, we have studied the spectral shift of the maxima observed in spectra, corresponding to EOT peaks, as a function of the medium refractive index. By this way, in case of biosensors, it is possible to detect biologic material immersed in a buffer. Because of immersions, buffer refractive index is slightly modified and spectral position of EOT peaks changes.

## 1.2 Surface plasmons

A plane wave consists on both an electric and a magnetic field vector, perpendicular to each other and to the propagation direction. Expressions for these fields are obtained through solving Maxwell's equations.

$$\vec{E}(\vec{r}) = \vec{E}_0 e^{i(\omega t - \vec{k}\vec{r} + \varphi_0)} \quad \vec{B}(\vec{r}) = \vec{B}_0 e^{i(\omega t - \vec{k}\vec{r} + \varphi_0)} \quad (1.1)$$

Metals are characterized by possessing free electrons in the conduction band even to low temperature, which are responsible for their high electric and thermal conductivity. Interaction between light and metals is the origin of surprising physical phenomena as plasmons.

The interaction of electromagnetic radiation with metals can be modeled through the Drude theory. This allows the knowledge of metals dielectric constants as a function of incident radiation frequency. So that, it provides their dispersion relations [4]:

$$\varepsilon_m(\omega) = 1 - \frac{\omega_p^2}{\omega(\omega + i\gamma)} \quad (1.2)$$

where  $\omega_p$  and  $\omega$  are the plasma and impinging light frequencies, and  $\gamma$  corresponds to damping time, which is related to energy losses by Joule's effect.

For  $\omega < \omega_p$ , refractive index is complex. Free electrons follow the external disturbance and oscillate to the same frequency as incident radiation, light does not propagate inside metal and is absorbed being attenuated in a few nanometers. However, for  $\omega_p < \omega$ , dielectric constant is real, electrons do not oscillate in phase with the field and, as a consequence, electromagnetic waves propagate through metal without being absorbed, as it occurs in dielectrics.

Under certain assumptions, surface plasmons (SP) can be generated. In this case, light propagates in the surface of the metal through evanescent waves, it can be seen in the Figure 1.1. Electromagnetic energy is confined to a bi-dimensional space.

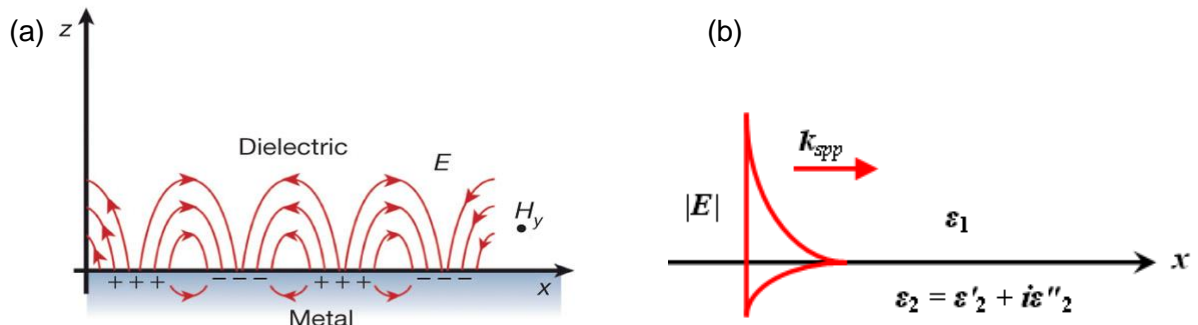


Figure 1.1: (a) Scheme of surface plasmons created at dielectric-metal interface. (b) Illustration of electric field in a metal-dielectric interface.

SP effect takes place at the interface between two media with opposite sign in the real part of their dielectric constant, a metal (negative) and a dielectric (positive). In infrared

and visible ranges, we talk about surface plasmons polaritons, which are coupled modes of a photon and a surface plasmon that propagate guided along interface as it occurs in an optical fiber. They are characterized by their wave vector [5], see Figure 1.2.

$$k_{SPP} = \frac{\omega}{c} \sqrt{\frac{\varepsilon_1 \varepsilon'_2}{\varepsilon_1 + \varepsilon'_2}} \quad (1.3)$$

being  $\omega$  the frequency of incident radiation,  $c$  the light speed in vacuum and  $\varepsilon_1$ ,  $\varepsilon'_2$  the dielectric constants for dielectric and metal (real part) respectively.

Taking into account that value of  $\varepsilon_2$  is given by the Drude model and considering the damping constant negligible, the maximum frequency for a surface plasmon polariton is given by:

$$\omega_{SPP} = \frac{\omega_P}{(1 + \varepsilon_1)^{\frac{1}{2}}} \quad (1.4)$$

In most of cases, dielectric medium is air, so that, equation 1.4 is simplified to the following value, which only depends on the plasma frequency of the considered metal (gold in this work), as it is represented in the following Figure.

$$\omega_{SPP} = \frac{\omega_P}{\sqrt{2}} \quad (1.5)$$

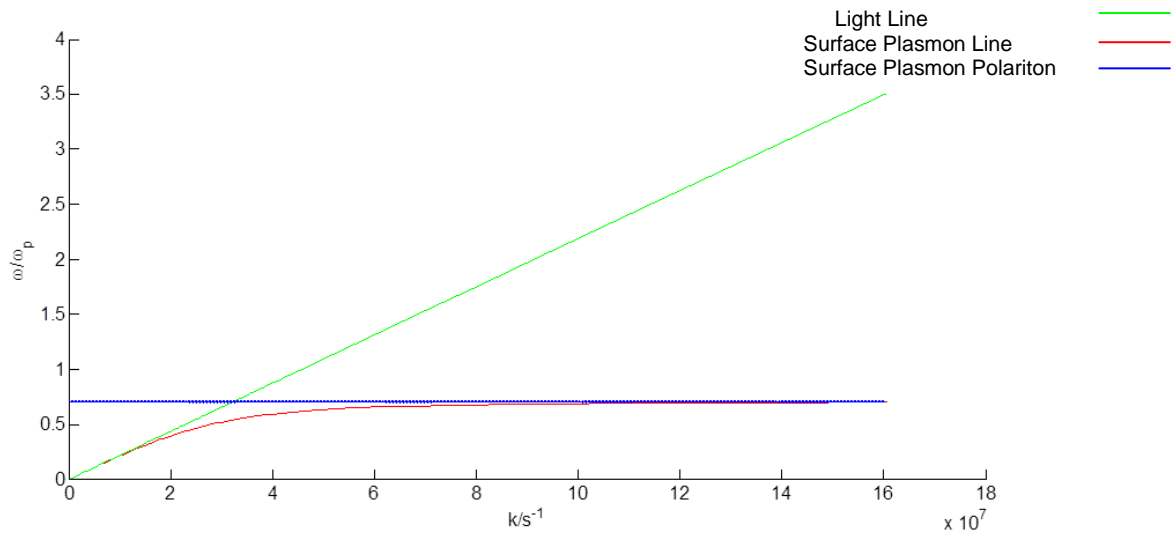


Figure 1.2: Dispersion relation for surface plasmons. Dielectric and metallic media correspond to air and gold respectively.

In the above Figure, it is observed that the dispersion curve corresponding to surface plasmons is below the light line, their wave number is always bigger than wave vector of photons in free space. In order to verify momentum conservation and excite surface plasmons with photons, it is necessary to draw on one of the following methods:

waveguides, grating coupler or attenuated total reflectance, which will provide to photons an extra-momentum.

An interesting SPP property is the absorption length,  $L_{abs}$ , which is defined as length at which the energy carried by the SPP decays in  $1/e$  [1].

$$L_{abs} = \lambda_0 \frac{(\varepsilon'_2)^2}{2\pi\varepsilon''_2} \left[ \frac{\varepsilon_1 + \varepsilon'_2}{\varepsilon_1\varepsilon'_2} \right]^2 \quad (1.6)$$

Figure 1.3 shows the SPP absorption length for air-gold. It must be noticed that for obtaining this expression the approximation for good metals ( $|\varepsilon'_2| \gg \varepsilon''_2$ ) has been considered.

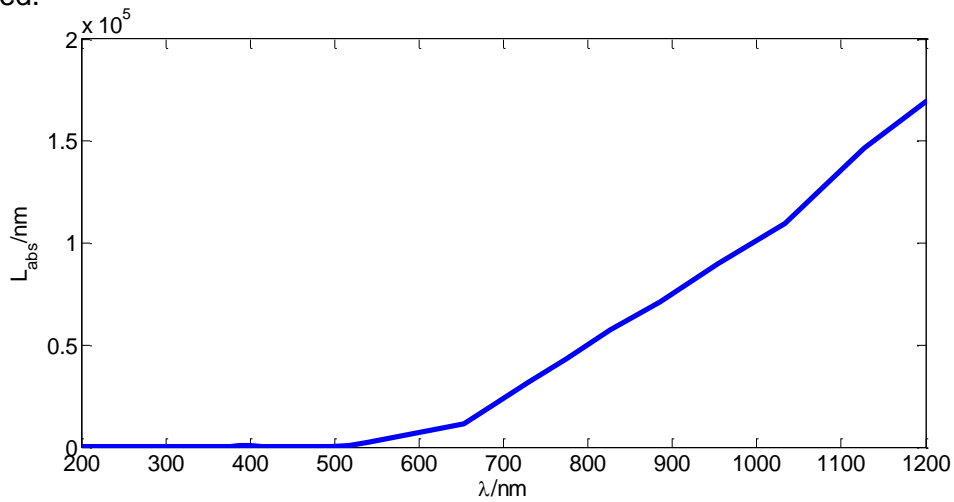


Figure 1.3: It is shown the SPP absorption length for air-gold (Au).

Another SPP property is its penetration into the dielectric,  $\delta_\varepsilon$ , and the metallic medium,  $\delta_m$ , Figure 1.4, which is given by the following expressions [1]:

$$\delta_\varepsilon \approx \frac{\sqrt{|\varepsilon'_2|} \lambda}{2\pi\varepsilon_1} \quad (1.7)$$

$$\delta_m \approx \frac{\lambda}{2\pi\sqrt{|\varepsilon'_2|}} \quad (1.8)$$

being  $\lambda$  wavelength of incident radiation.

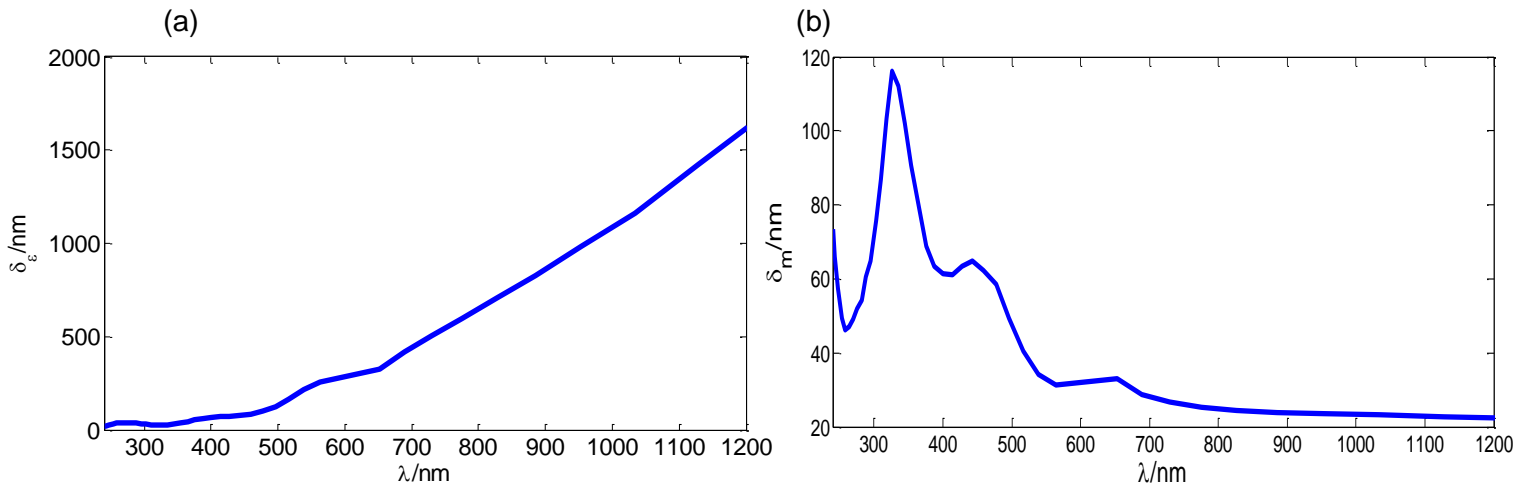


Figure 1.4: Skin depth inside (a) dielectric, air and (b) metal, gold (Au).

Comparing Figures 1.3 and 1.4(a), it is observed that both exhibit the same trend. In Figure 1.4(a), we see how the plasmon only penetrates into the dielectric medium about 300-500nm in the visible range (400-700nm). This supposes that, for biosensors, the effective distance where changes in the refractive index can be observed corresponds with the values mentioned before.

### 1.2.1 Different configurations for exciting surface plasmons

Before using nanostructured systems, much effort was done by different scientists in the middle of last century in order to excite surface plasmons with light (photons), which need an extra-momentum in order to move from the light line to the plasmons dispersion curve. This goal was achieved through different experimental configurations, some of the most important are: Grating, Otto and Kretschmann configurations, Figure 1.8. All of them are based on total internal reflection.

Snell's law establishes that total internal reflection will be given for incident angles larger than the critical angle,  $\varphi_L$ . In those cases  $\sin(\varphi') > 1$ .

$$n \sin(\varphi) = n' \sin(\varphi') \quad \begin{matrix} \varphi = 90^\circ \\ \Rightarrow \end{matrix} \quad \sin(\varphi_L) = \frac{n'}{n} \quad (1.9)$$

where  $n$  and  $n'$  are refractive indexes of both media, which can be observed in Figure 1.5.

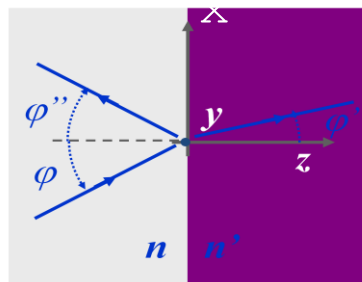


Figure 1.5: Geometry of the incident plane

Applying the Pythagorean trigonometric identity, we get an expression for  $\cos(\varphi')$

$$\cos \varphi' = \sqrt{1 - \sin^2 \varphi'} = \sqrt{\text{Negative}} \equiv [\text{Imag. number}] \Rightarrow \cos \varphi' = -i \frac{n}{n'} \sqrt{\sin^2 \varphi - \left(\frac{n'}{n}\right)^2}$$

Hypothesizing that Fresnel's equations are valid for complex numbers, for parallel and perpendicular polarizations the following expressions are obtained for reflected waves, [6]:

$$A_{\perp}'' = \frac{\cos \varphi + i \sqrt{\sin^2 \varphi - N^2}}{\cos \varphi - i \sqrt{\sin^2 \varphi - N^2}} A_{\perp} \quad A_{\parallel}'' = -\frac{N^2 \cos \varphi + i \sqrt{\sin^2 \varphi - N^2}}{N^2 \cos \varphi - i \sqrt{\sin^2 \varphi - N^2}} A_{\parallel} \quad (1.10)$$

where  $N = \frac{n'}{n}$  and  $A_{\parallel}''$ ,  $A_{\perp}''$ ,  $A_{\parallel}$ ,  $A_{\perp}$ , are parallel and perpendicular to the incident plane reflected ("") and incident amplitudes of electric field, respectively.

By this way, complex reflection coefficients, whose module is 1, are obtained. Thus total internal reflection transmission is zero.

The transmitted wave, considering the incident field as a plane wave, is given by [6]:

$$\vec{E}' = \vec{A}' e^{i \frac{\omega}{c} [ct - nx \sin \varphi]} e^{i^2 \frac{\omega}{c} n' \frac{1}{N} \sqrt{\sin^2 \varphi - N^2} z} \quad (1.11)$$

Where  $\vec{A}'$  is the amplitude of the transmitted wave.

As it can be observed through equation 1.11, transmitted wave corresponds with an evanescent wave, which for the considered geometry decays exponentially in z direction and propagates in x.

Analyzing reflection coefficients and factors, Figures 1.6 and 1.7 respectively, it is found as reflection is equal to unit (considering non-absorbing media) for angles greater than critical angle, which is consistent with the fact that in transmission we only observe evanescent waves.

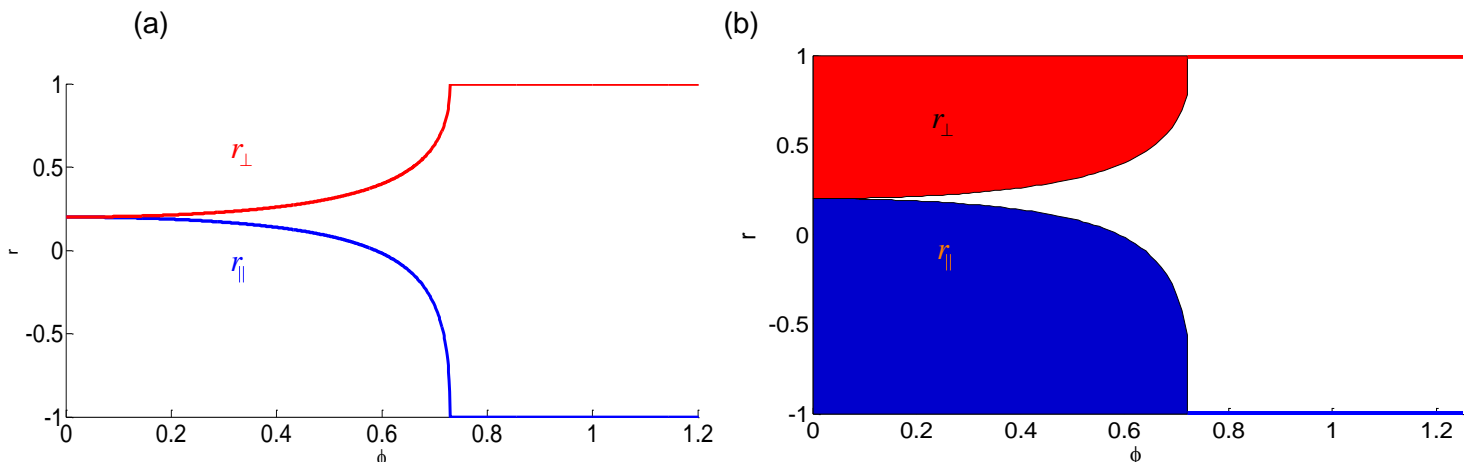


Figure 1.6: It is shown reflection coefficient for  $n=1.5$  and  $n'=1$  as a function of incident angle. In (b) shadow areas correspond to angles lower than the critical angle.

As it is represented in Figure above, for angles greater than the critical angle, reflection coefficient is equal to 1 for parallel/perpendicular to the incident plane electric field components. Because of these values, reflection factor will be equal to 1 (see Figure 1.7), which means, light will not be transmitted at all.

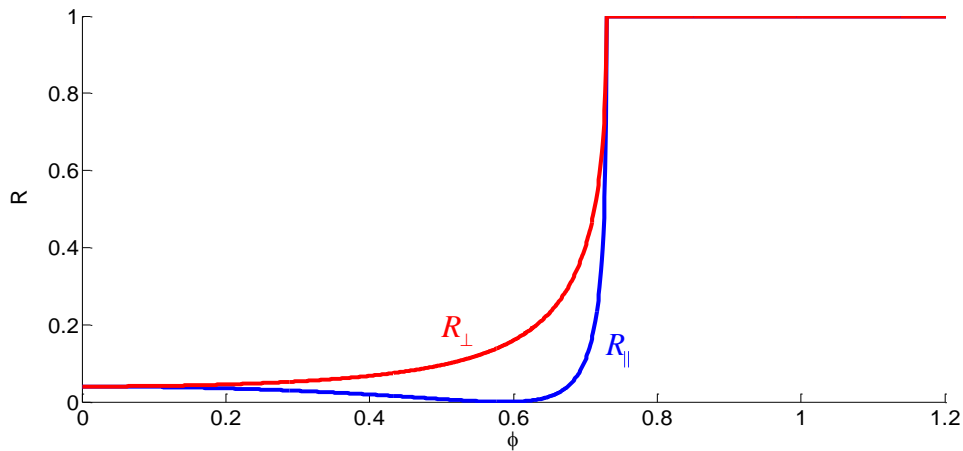


Figure 1.7: Reflection factor for  $n=1.5$  and  $n'=1$  as a function of incident angle.

- **Grating configuration:**

In this configuration, Figure 1.8 (a), a corrugated structure is used in order to provide photons the needed extra-momentum that was discussed in the analysis of Figure 1.2. It is supposed that light travels from air,  $\epsilon_1=1$ , to a grating characterized by a constant, spatial period, equal to  $b$ . By this way, parallel to grating wave vector is increased by the following factor:  $\Delta k = \frac{2\pi}{b}$  and surface plasmons can be excited for a certain incident angle,  $\theta_0$ , at which equation 1.13 is fulfilled, [7].

$$\frac{\omega}{c} \sin \theta_0 + \frac{2\pi}{b} = \frac{\omega}{c} \sqrt{\frac{\epsilon_2}{1+\epsilon_2}} \quad (1.13)$$

Although its theoretical basis is quite simple, this configuration is not very useful because light must go through sample, which can generate some inaccuracies in measurements.

- **Otto configuration:**

Incoming light goes across a glass prism with dielectric constant  $\epsilon_0$ , which is separated from a metallic surface,  $\epsilon_2$ , by a dielectric medium, mostly air,  $\epsilon_1$ , as it is observed in Figure 1.8 (b). For certain incident angles, internal total reflection is achieved and, as a consequence, evanescent waves appear, exciting surface plasmons at the dielectric-metal surface.

In this case, surface plasmons will be excited when equation 1.14 is accomplished, [7]:

$$\frac{\omega}{c} \sqrt{\epsilon_0} \sin \theta_0 = \frac{\omega}{c} \sqrt{\frac{\epsilon_1 \epsilon_2}{\epsilon_1 + \epsilon_2}} \quad (1.14)$$

- **Kretschmann configuration:**

This configuration is really similar to the explained above, the most remarkable differences between both of them is that, in the last one, prism is set on a thin metal film and surface plasmons will be created at the interface metal-dielectric (no dielectric-metal), as it can be observed in Figure 1.8 (c).

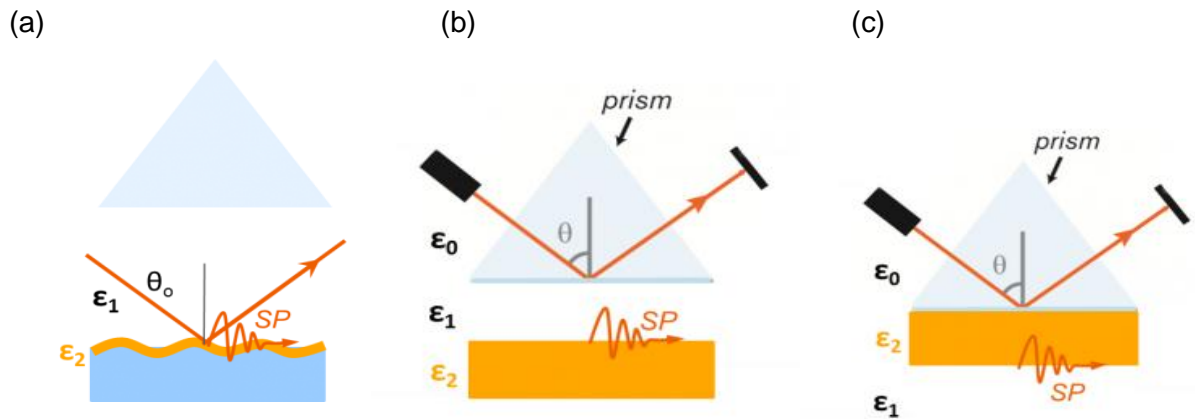


**Figure 1.8:** Different configurations for exciting surface plasmons. (a) Grating configuration, (b) Otto configuration, (c) Kretschmann configuration.

Experimentally, in the three considered cases, when the resonant condition is obtained, a minimum is observed in the reflection spectrum. This behavior can be explained through Fresnel's equations.

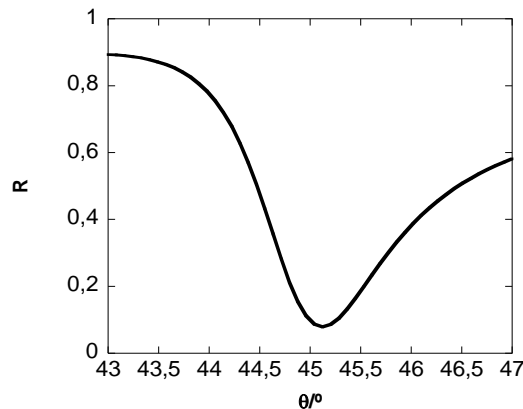


**Figure 1.9:** Reflection at gold film of thickness 60nm,  $\lambda=634\text{nm}$ .

For the case of the Kretschmann configuration reflection factor in the resonance region can be approximated by, [5]:

$$R \approx 1 - \frac{4\Gamma_i \Gamma_{rad}}{[k_x - (k_x^0 + \Delta k_x)]^2 + (\Gamma_i + \Gamma_{rad})^2} \quad (1.15)$$

where  $k_x = \sqrt{\varepsilon_0} \frac{\omega}{c} \sin(\theta_0)$  ,  $k_x^0 = \frac{\omega}{c} \sqrt{\frac{\varepsilon_1}{\varepsilon_1 + 1}}$  ,  $\Gamma_i = \text{Im}(k_x^0)$  ,  $\Gamma_{rad} = \text{Im}(\Delta k_x)$  and

$$\Delta k_x = \left[ \frac{\omega}{c} \frac{2}{1 + |\varepsilon'_1|} \left( \frac{|\varepsilon'_1|}{|\varepsilon'_1| - 1} \right)^{3/2} \exp(-2|k_x^0 d_1|) \right] r_{01}^p(k_x^0)$$

corresponding  $\varepsilon'_1$  with the real part of dielectric constant in metal,  $d_1$  with thickness of

metal film and  $r_{01}^p$  with:  $r_{01}^p = \frac{\left( \frac{k_{z0}}{\varepsilon_0} - \frac{k_{z1}}{\varepsilon_1} \right)}{\left( \frac{k_{z0}}{\varepsilon_0} + \frac{k_{z1}}{\varepsilon_1} \right)}$

The commented minimum is achieved for  $\Gamma_i = \Gamma_{rad}$  .

With nanotechnology development, new ways of exciting surface plasmons have been proposed. Some of the most popular are based on manufacturing periodic nanostructures where periodicity will be responsible for the extra-momentum. However, these nanostructures present lower sensitivities than the based on total internal reflection, [8].

Some of the most typical examples found in literature are based on the use of nanoparticles on a metallic structure surface, Figure 1.10, or nanoholes perforated in a thin metallic film, as in the case of this project. Particularly, for square lattices of nanoholes, excitation of surface plasmons by light in a periodic nanostructure will be observed when the following condition is accomplished, [9]:

$$\vec{k}_{SP} = \vec{k}_x \pm i\vec{G}_x \pm j\vec{G}_y \quad (1.16)$$

being  $\vec{k}_x$  wave vector of incident radiation in x-direction, i and j integer numbers corresponding to orders of reciprocal lattice, whose vectors are  $\vec{G}_x$  ,  $\vec{G}_y$  and their modulus are given by these expressions:

$$|\vec{G}_x| = |\vec{G}_y| = \frac{2\pi}{P} \quad (1.17)$$

where P is the lattice periodicity.

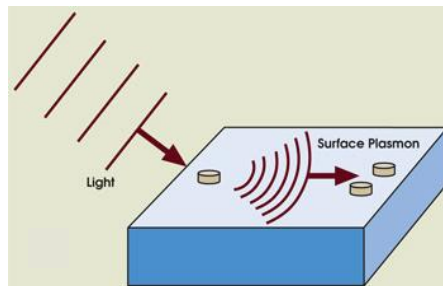


**Figure 1.10:** Nanostructured system used for formation of surface plasmons.

## 2.1 Objectives

In the present work we have studied interaction of electromagnetic radiation with different periodic nanostructured systems (metallic thin films with nanoholes). This project has been motivated by numerous applications that these systems present: biomedicine, biosensors...In fact, the main objective of the work is designing a biosensor easy to manufacture and where sensitivity was high.

For carrying out this aim, it is necessary to study transmission spectra of a simulated nanostructured thin metallic film, which is set on a dielectric substrate. On this film, it is found a buffer of known refractive index, where biological material is immersed in. As a consequence of computational problems associated to lack of memory, it is not possible to solve the problem in 3-D, so that, we decided to modelize it in 2-D, obtaining a similar behavior.

The obtained results simulating immersions inside the buffer were compared with those gotten using the refractive index effective medium theory. Achieved spectra by both methods were in very good agreement. After proving such verification, it was decided to use this theory for carrying out the rest of results in the project.

During the work, we studied different configurations in order to reach high sensitivity to changes in the buffer refractive index. All of them were simulated with COMSOL.

## 2.2 Work scheme

Firstly, we have done a review of literature concerning the topics that refer to this project. In the following sections the main fundamentals of the different theories commented before are shown, as well as, several applications of biosensors. In the last sections, results with the most relevant conclusions can be found. In order to understand different theoretical aspects related to surface plasmons, some programs have been created with MATLAB. Through them we can observe the main features that govern the behavior of this physical phenomenon.

In case of 2-D simulations, the following situations have been considered:

- Gold nanoslit array, set on a dielectric substrate (glass). On this structure a buffer is set, characterized by an effective refractive index.
- Gold nanoslit array, set on a dielectric substrate (glass). On this structure it can be observed an object (which simulates biologic material) immersed in a buffer corresponding to water. Object is fixed to gold nanostructure.
- The same configuration as in the above point, but, in this case, object is floating in water, separated by a few nanometers of the gold grating surface.

In case corresponding to the first point, buffer refractive index was changed from 1.33 to 1.34 with steps of 0.002. In the second one, number of “objects” was varied for observing the correspondence between these results and the concerning ones to change the medium refractive index. In the last point, only one “object” was considered. It was moved in the transversal to the grating axis, in order to observe how spectrum changes with the position of the object respect to grating.

For 3-D simulations, effective medium theory has been applied and different geometries, which will be explained in the results section, have been studied. In all of them sensitivity has been calculated.

## Diffraction theory

Diffraction is a physical phenomenon, which is revealed when light goes through an aperture, or equivalently, an obstacle. Waves are spread in all directions. It is an intrinsic characteristic to waves and is mostly observed when apertures size is comparable to the wavelength of incident radiation (in case of light). In the following section we are doing a brief review of Fraunhofer and Fresnel diffraction theories.

Kirchhoff in 1882 proposed the scalar diffraction theory, from which, it is possible to obtain Fresnel and Fraunhofer theories.

It is supposed a punctual source that emits scalar, monochromatic waves, and the main objective is to know complex amplitude of electric field in a concrete point, P, as it is represented in Figure 3.1 (a).

Electric field emitted by the source is given by:

$$E = \frac{E_0}{r_s} e^{-ikr_s} e^{i\omega t} \quad (3.1)$$

where  $r_s$  is the radial coordinate from the source. Complex amplitude is written in red, which in P is expressed as, [10]:

$$(E_C)_P = \frac{1}{4\pi} \int_{\Sigma} \left[ \frac{1}{r} e^{-ikr} \frac{\partial E_C}{\partial N} - E_C \frac{\partial}{\partial N} \left( \frac{1}{r} e^{-ikr} \right) \right] d\Sigma \quad (3.2)$$

N corresponds to the normal direction in each point of the closed surface and r corresponds with distance from P to each point of it.

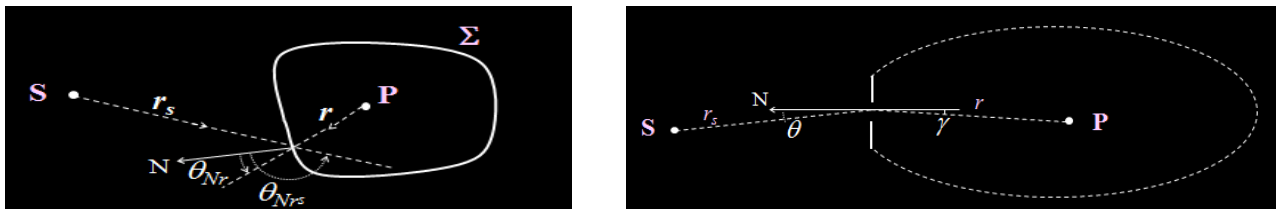


Figure 3.1: (a) Scheme used for calculating Kirchhoff diffraction integral, (b) Diffraction by an aperture.

The typical diffraction scheme by an aperture is shown in Figure 3.1 (b), where it is defined an arbitrary  $\Sigma'$ .  $(E_C)_P$  is null in all points, except in the corresponding ones to the aperture,  $\Sigma'$ . So that,  $(E_C)_P$  is expressed as:

$$(E_C)_P = \frac{ikE_0}{4\pi} \int_{\Sigma'} \frac{1}{rr_s} e^{-ik(r+r_s)} [\cos(\gamma) + \cos(\theta)] d\Sigma' \quad (3.3)$$

With the objective of obtaining the expressions corresponding to Fresnel and Fraunhofer diffraction, coordinate origin is considered in the aperture as it can be observed in Figure 3.2.

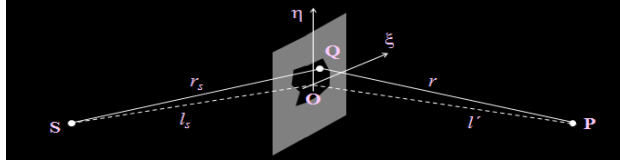


Figure 3.2: Diffraction scheme, origin coordinate is set in the own aperture.

For the particular case, where distances  $l_s$  and  $l'$  are big compared with  $\overline{OQ}$ , terms  $\frac{1}{rr_s}$  and  $\cos(\gamma) + \cos(\theta)$  remain constant. Also, it is possible to express  $r_s$  and  $r$  as an infinite sum of terms, and take only the first one, [6].

Taking into account these approximations, valid when observer and source are at “infinite” respect to diffracting aperture, Fraunhofer diffraction, equation 3.3 is expressed as:

$$(E_C)_P = \frac{ikE_0[\cos \gamma + \cos \theta]}{4\pi r_s r} e^{-ik(l_s+l')} \int_{\Sigma'} e^{-ik[(\alpha-\alpha')\xi+(\beta-\beta')\eta]} d\xi d\eta \quad (3.4)$$

where  $r_s+r$  has been approximated by:  $r_s + r \cong (l_s + l') + (\alpha - \alpha')\xi + (\beta - \beta')\eta$  and  $\alpha, \alpha', \beta$  and  $\beta'$  are given by:  $\alpha = -\frac{x}{l_s}$ ,  $\alpha' = \frac{x'}{l'}$ ,  $\beta = -\frac{y}{l_s}$ ,  $\beta' = \frac{y'}{l'}$ , which are known as cosine directors.

If distances from S and P to origin ( $l_s, l'$ ) are not enough big, more terms of the series should be included, in this case, we talk about Fresnel diffraction.

Due to in this project we have simulated nanoholes with circular shape, it is important to review Fraunhofer diffraction by a circular aperture.

Amplitude of electric field in a point P of a lens focal plane, which is set behind aperture, corresponds to:

$$(E_C)_P = 2\pi C \frac{Rf'}{k\rho'} J_1\left(\frac{k\rho'R}{f'}\right) \quad (3.5)$$

where R is the aperture radius,  $f'$  the image focal length of the used lens (convergent),  $\rho'$  the radial coordinate in the image focal plane and C a constant.  $J_1$  refers to Bessel function of first order.

Intensity is represented by the Airy function, which is characterized by showing a maximum for  $\rho'$  equal to zero and periodic null minima (rings), as it can be observed in Figure 3.3.

$$I \propto \left( \frac{2J_1(z)}{z} \right)^2 \propto \frac{1}{z^2} \propto \frac{R^2}{\lambda^2} \quad (3.6)$$

being  $z = \frac{k\rho'R}{f'}$

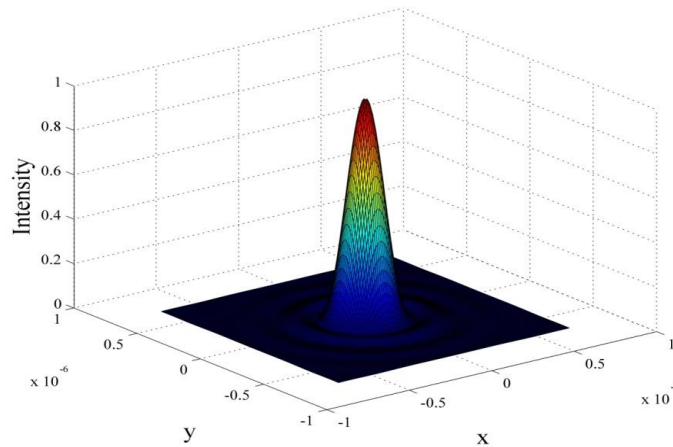


Figure 3.3: Airy disk, intensity pattern by a circular aperture.

For periodic nanohole arrays, incident light is diffracted by infinite apertures. So, intensity pattern is the result of interference of diffracted waves by each one of nanoapertures. Constructive interference will be found when the following equation, Bragg's law, is fulfilled.

$$P \sin(\theta) = n\lambda \quad (3.7)$$

where P corresponds with lattice period,  $\theta$  is the incidence angle and n is an integer number, known as diffraction order.

As can be observed through the equation above, it is not possible to find radiative diffraction orders for wavelengths greater than the period. So that, resonances in spectra are attributed to another physical phenomenon, EOT, which is associated to surface plasmons, as it will be explained in the following section.

### 4.1 Origin of Extraordinary Optical Transmission

Light transmission through circular holes can be explained by diffraction theory, see section 3. Most of theories in the last century established a proportional (inverse) quadratic dependence of transmission with hole radius (wavelength of incident radiation),  $(R/\lambda)^2$ , eq (3.6). Bethe's contribution, in 1944 to this topic, supposed a revolution. He proposed that transmission by a hole perforated in a metallic thin (thickness  $\ll \lambda$ ) film, considered as perfect conductor, was given by, [1]:

$$T = \frac{64}{27\pi^2} \left(\frac{R}{\lambda}\right)^4 \quad (4.1)$$

It is valuable to notice that in this expression, transmission is normalized to hole area.

Through equation 4.1 it is observed that transmission by nanoholes is really low, see Figure 4.1.

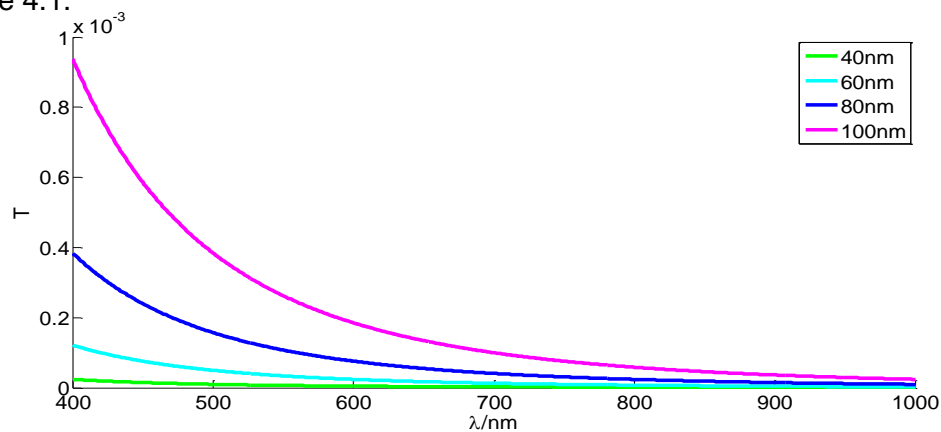


Figure 4.1: Transmission for different nanohole sizes.

Through Figure 4.1 we observe as transmission is really low, being slightly greater for the biggest radiuses and the lowest wavelengths. The described behavior is the expected one from the Bethe's description.

However, it was observed that transmission through this kind of metallic nanostructures was really high. It supposed the discovery of Extraordinary Optical Transmission (EOT). This phenomenon takes place in 2-D periodic nanohole arrays, which are perforated in thin metallic films. Due to nanotechnology development, this kind of nanostructured systems can be manufactured and used in many applications, essentially as biosensors.

Mechanism that governs behavior of EOT is intimately related to excitation of surface plasmon polaritons (SPP). In fact, nowadays, it is attributed to interaction of SPP that take place in each of the metal film surfaces. For this reason, it is necessary that thickness of metal film is not greater than 2-3 skin depths, as it was presented in Figure 1.4 (a) of section 1.2. Due to periodicity of nanohole array film modes appear. They are characterized by different dispersion relations to the corresponding to surface plasmons.

Film modes will appear to the following wavelengths, [11]:

$$\lambda_{SPP} = \frac{P \sqrt{\frac{\epsilon_1 \epsilon_2}{\epsilon_1 + \epsilon_2}}}{\sqrt{n^2 + m^2}} \quad (4.2)$$

P is the grating period of a symmetric lattice,  $\epsilon_1$  and  $\epsilon_2$  refer to dielectric constants of dielectric and metal respectively and “n”, “m” are integer numbers which characterize the transmission mode.

In the case of symmetric rectangular nanoholes, the relation dispersion is given by, [1]:

$$q^2_{\text{mode}}(\lambda) = (k_x^{\text{in}} + \frac{2\pi n}{P})^2 + (k_y^{\text{in}} + \frac{2\pi m}{P})^2 \quad (4.3)$$

where  $k_x^{\text{in}}$  and  $k_y^{\text{in}}$  correspond to wavevectors of incident radiation in the metallic thin film plane.

For this particular case and normal incidence,  $k_x^{\text{in}}$  and  $k_y^{\text{in}}$  are equal to zero, so equation 4.3 is reduced to:  $q^2_{\text{mode}}(\lambda) = (\frac{2\pi n}{P})^2 + (\frac{2\pi m}{P})^2$ , see Figure 4.2.

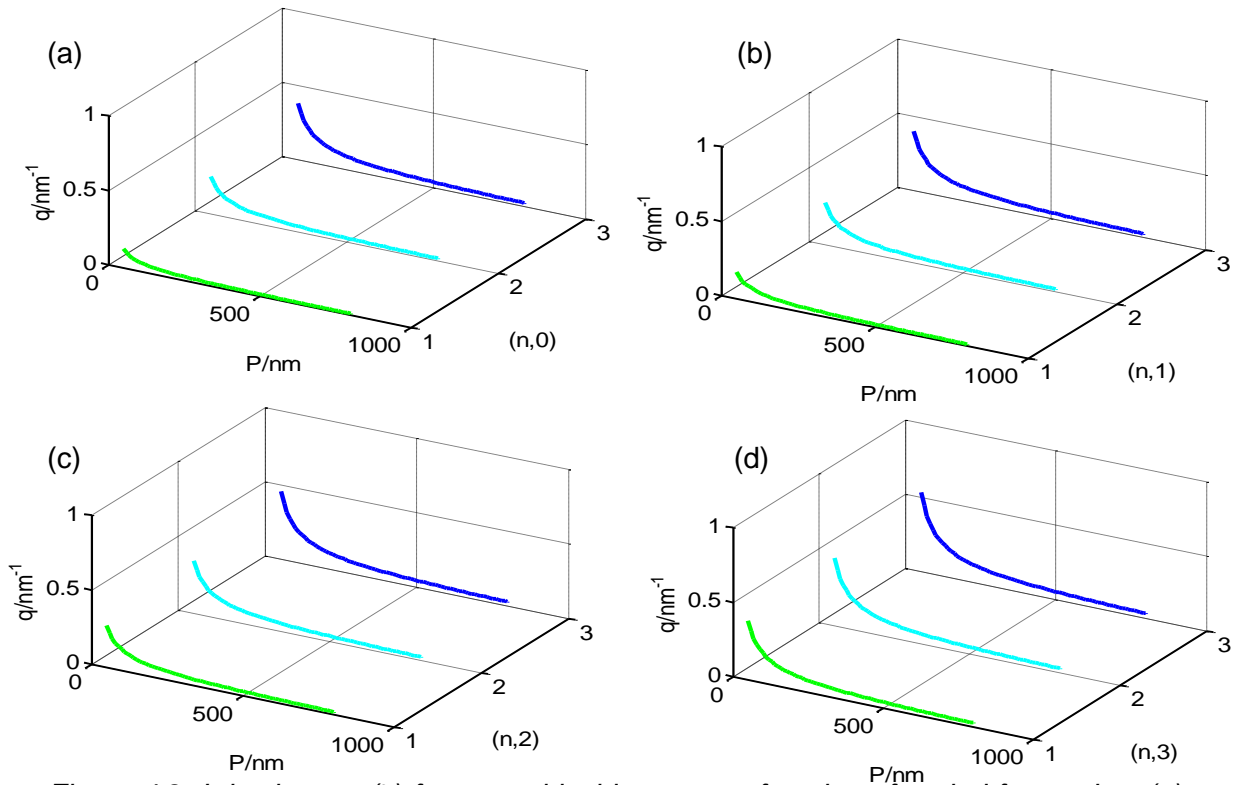


Figure 4.2: It is shown  $q(\lambda)$  for normal incidence as a function of period for modes: (a)  $(n,0)$ , (b)  $(n,1)$ , (c)  $(n,2)$  and (d)  $(n,3)$ , where  $n$  varies from 1 to 3 in all panels.

In Figure 4.2 it is observed as  $q(\lambda)$  increases with  $n$  and  $m$  and decreases with period, as it was expected from equation 4.3.

Subscript “mode” refers to SPP or SRSP (Surface Plasmon Polariton Short Range) or LRSP (Surface Plasmon Polariton Long Range) as appropriate.

It is possible to distinguish two different modes, each one of them characterized by its relation dispersion, symmetric (LRSP, denoted by superscript +) and antisymmetric (SRSP, denoted by subscript -), [12]. They appear as a consequence of interference between surface plasmons at the two surfaces dielectric-metal, [13]. The most important difference between these surface plasmons is the propagation distance. In the case of SRSP, attenuation is high and propagation length is short. For LRSP, the opposite behavior is given.

Dispersion relations for LRSP and SRSP are given by equation 4.4 left and right respectively, [14]:

$$\tanh\left(\frac{\alpha_2 d}{2}\right) = -\frac{\varepsilon_2 \alpha_1}{\varepsilon_1 \alpha_2} \quad \tanh\left(\frac{\alpha_1 d}{2}\right) = -\frac{\varepsilon_1 \alpha_2}{\varepsilon_2 \alpha_1} \quad (4.4)$$

where  $\varepsilon_1$ ,  $\varepsilon_2$  are dielectric and thin film permittivities,  $d$  corresponds to the thickness of film and  $\alpha_1$ ,  $\alpha_2$  are related with  $\varepsilon_1$ ,  $\varepsilon_2$ ,  $k_0$  (wave vector in vacuum) and  $k$  (propagation constant in x-direction) by:  $\alpha_1^2 = k^2 - k_0^2 \varepsilon_1$ ;  $\alpha_2^2 = k^2 - k_0^2 \varepsilon_2$ .

Another important factor to take into account is how surface plasmons at both interfaces are able to couple. In literature, it is found two different ways: through their evanescent character and through the Fabry-Perot effect. For symmetric modes, they are coupled by the first commented mechanism, which depends on the periodicity of the considered structure. In the case of antisymmetric coupling, Fabry-Perot resonance inside hole is responsible for interaction between surface plasmons. It is not as greatly dependent on period as on nanohole properties. Evanescent waves, Fabry-Perot resonance are the main coupling mechanisms for small and large nanohole apertures respectively, [13].

For small holes, the periodicity of nanostructure determines the behavior of EOT, which is due to relation between resonant EOT peaks and SPP Bloch modes in the structure. For larger holes, relation between EOT peaks and Bloch modes is not always verified, because coupling between both interfaces metal-dielectric is by Fabry-Perot resonance. In this case, it will be determined by the holes depth, but in any case by periodicity.

Apart from periodicity structure and nanohole characteristics, there are several properties that determine EOT resonance of nanostructured systems: materials, nanohole shape...

## 4.2 Role of materials in EOT

Material that thin films are made of, plays an important role in features of transmission spectra, so that, it deserves special attention.

As it was commented before (section 1.2) the behavior of metals with electromagnetic radiation can be explained through Drude’s model. Dielectric constants used during this

project have been obtained from Palik's handbook [15] and are represented in Figure 4.3 for Au, Ag, Cu, Cr and Ni.

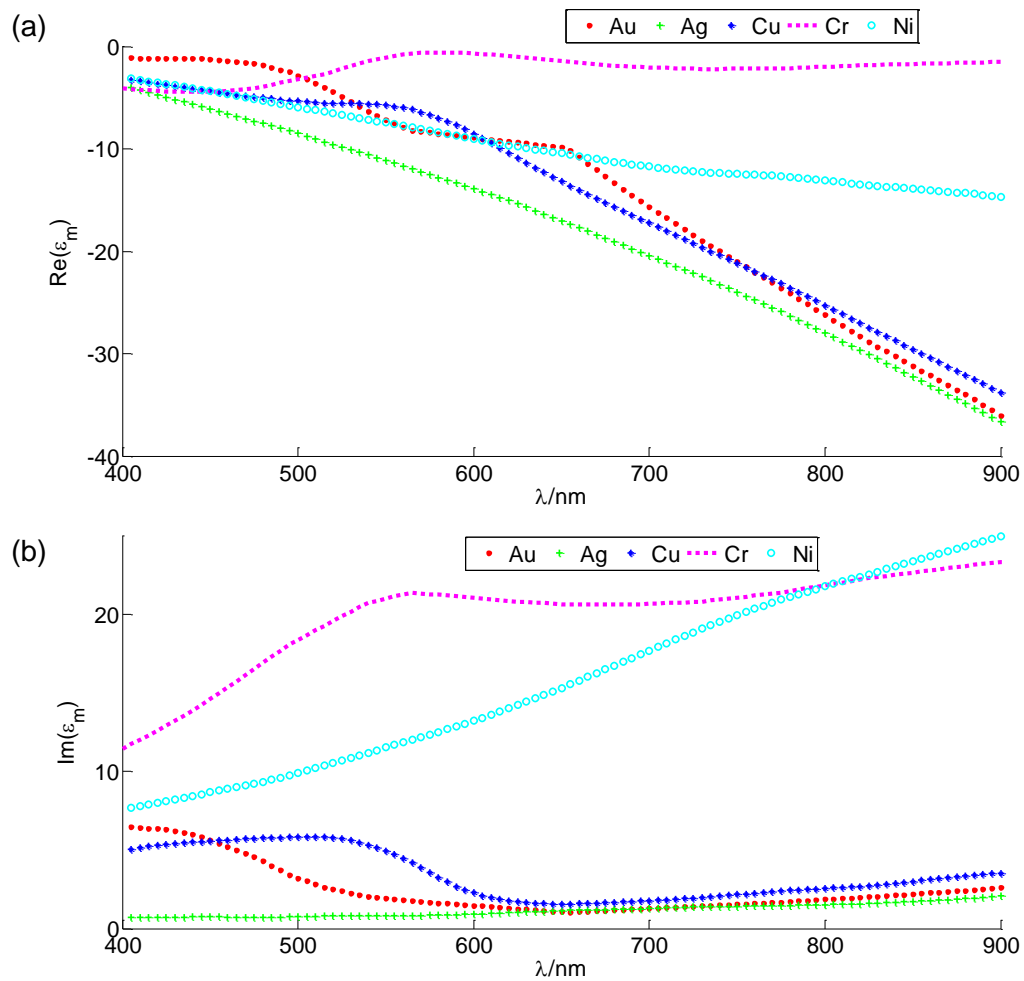
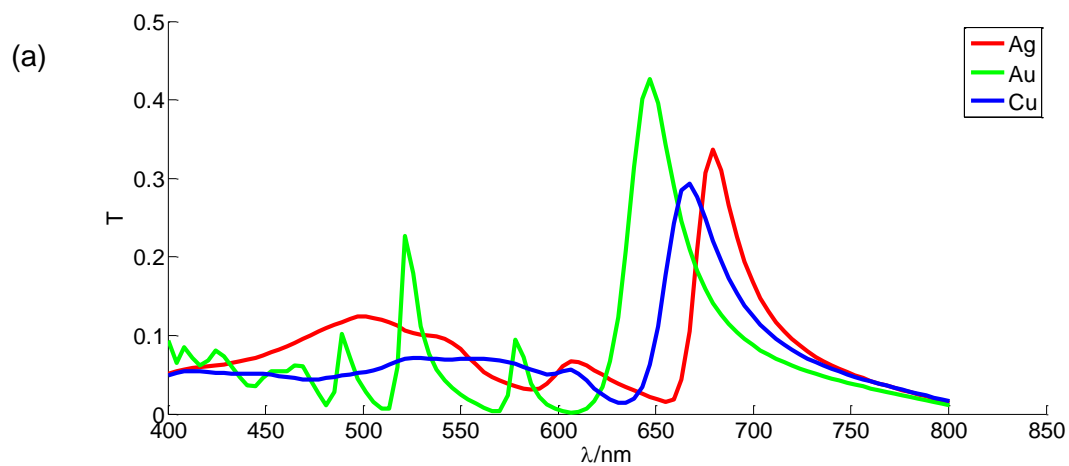


Figure 4.3: Dielectric constants of different metals. In panels (a) and (b) real and imaginary parts of dielectric constants are shown, respectively.

In analogy to research carried out in [1], we have obtained transmission spectra for different metals with the objective of comparing resonance peaks, see Figure 4.4.



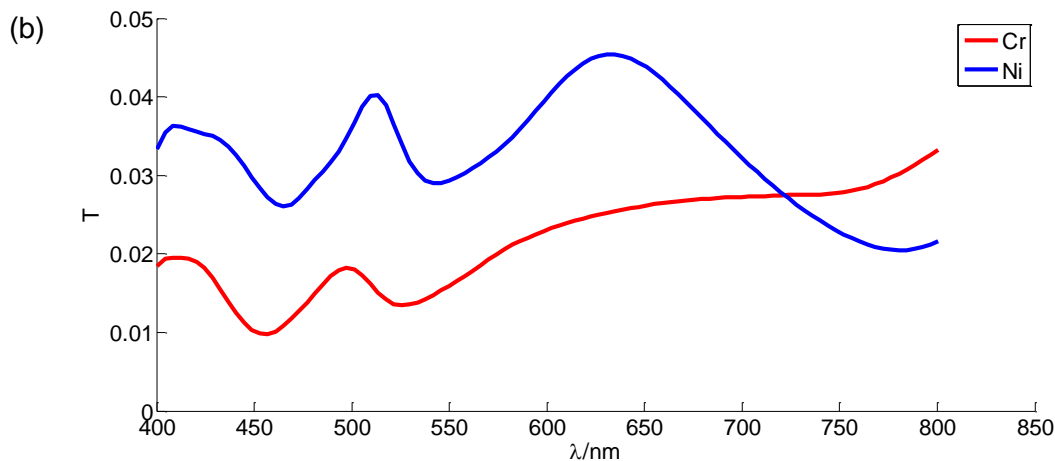


Figure 4.4: Transmission spectrum for different metals (a) “good” metals, (b) “bad” metals.

From Figure 4.4 it is observed that resonances take the highest values for good metals, like Ag or Au. Also, depending on the considered metal, resonance takes different spectral position.

Transmitted intensity in case of metals depends on two different factors: absorption and effective area, which modify the transmission in an opposite way, [1]. Imaginary part of dielectric constant is responsible for absorption, which originates that transmission decreases. Otherwise, in metals, electric field penetrates a few nanometers inside the structure, and consequently, the effective area of nanohole increases. This fact can be visualized in transmission spectra as higher peaks. By this way, it is put in evidence as material influences transmittance. In order to know the mechanism that contributes more efficiently, several projects compare the obtained spectrum for a metallic nanostructure with the corresponding to a Perfect Electric Conductor (PEC), where absorption is null. If transmission of “real” metal is higher than that corresponding to PEC, effective area contribution is the most important mechanism. In order to corroborate this idea, nanoholes area in PEC is multiplied by a factor, skin depth of considered metal. As general trend, it is observed as in good metals the predominant factor is effective area, while for bad metals, like Ni or Cr, the most important one is absorption, although skin depth is even greater than in case of good metals, Ag or Au.

Another interesting question is the dependence of width peak with the metallic material. In case of good metals, absorption is lower than for bad metals, this implies that lifetime of surface plasmons will be greater and, consequently, narrower peaks will be found in spectrum, (full width half maximum (FWHM) and lifetime are inversely proportional).

### 4.3 Role of nanohole shape in EOT

Depending on nanohole shape, transmission spectra experiment different changes, which are underlined in height and spectral position of resonant peaks. Apart from, circular shape, EOT has been explored in different perforated nanostructures, the most

common, due to their high sensitivity, are rectangular and elliptical, [16] shapes. In this section we show transmission expressions for rectangular nanoholes, which have been obtained using the Coupled Mode Method, [1]. This is based on representing electric field as a combination of plane waves and applying the corresponding boundary conditions.

In Figure 4.5 we observe a scheme of this kind of structures.

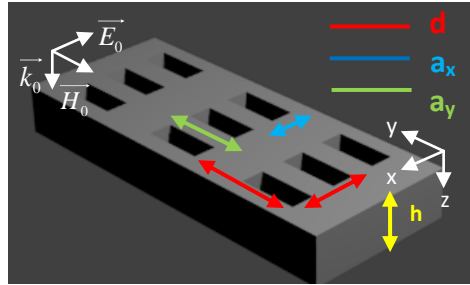


Figure 4.5: Scheme of a 2-D rectangular nanohole array illuminated at normal incidence with an x-polarized plane wave.

$$T = \frac{|I_0|^2}{4\sqrt{\varepsilon}} \frac{G_i}{(G_i)^2 + \left(\frac{|G - \Sigma|^2 - |G_v|^2}{2|G_v|}\right)^2} \quad (4.5)$$

where  $I_0$  represents the superposition of incident radiation (plane wave) and 0-mode inside hole and is given by the following expression:

$$I_0 = \frac{i4\sqrt{2}}{\pi(1+Z_s)} \sqrt{\frac{a_x a_y}{d_x d_y}}$$

(4.6)  $Z_s$  corresponds with surface impedance:  $Z_s = \frac{1}{\sqrt{\varepsilon_m}}$  being  $\varepsilon_m$  metal dielectric

constant, and  $a_x$ ,  $a_y$ ,  $d_x$  and  $d_y$  are hole size and period in x and y-axis respectively, see Figure 4.5.

$G_v$  gives idea about coupling between both sides of holes, its equation is:

$$G_v = \frac{2iY_0 e^{iq_z h}}{e^{iq_z h} (1+Z_s Y_0)^2 - (1-Z_s Y_0)^2} \quad (4.7)$$

where  $Y_0 = q_z/k_0$  ( $k_0 = 2\pi/\lambda$ ),  $q_z = \sqrt{\varepsilon_{hole} g^2 - q_y^2}$  ( $q_y = \pi/a_y$ ,  $\varepsilon_{hole}$  is the electric permittivity inside hole, [17]),  $g = 2\pi/\lambda$  and  $h$  is the metal thickness.

$$\Sigma = iY_0 \frac{e^{2iq_z h} (1+Z_s Y_0) + (1-Z_s Y_0)}{e^{2iq_z h} (1+Z_s Y_0)^2 + (1-Z_s Y_0)^2} \quad (4.8)$$

G term is responsible for electromagnetic coupling between plane waves corresponding to hole and continuum.

$$G = \frac{ia_x a_y}{2d_x d_y} \sum_{l=-\infty}^{l=+\infty} \sum_{m=-\infty}^{m=+\infty} \frac{k_0(k_0 + Z_s k_z) - k_m^2}{(k_z + Z_s k_0)(k_0 + Z_s k_z)} \text{sinc}^2\left(\frac{k_l a_x}{2}\right) \left[ \text{sinc}\left(\frac{k_m a_y + \pi}{2}\right) + \text{sinc}\left(\frac{k_m a_y - \pi}{2}\right) \right]^2 \quad (4.9)$$

where  $k_l = \frac{2\pi}{d_x} l$ ,  $k_m = \frac{2\pi}{d_y} m$ ,  $k_z = \sqrt{k_0^2 - k_p^2}$  and  $k_p = \sqrt{k_l^2 + k_m^2}$

#### 4.4 Different nanostructures

Due to use of EOT in biosensors, different nanostructures have been designed in order to improve their sensitivity. In the following section we do a brief review about the most important ones.

In the above section, it was shown the role of nanohole shape in EOT. Recently, different papers describing transmission through elliptical nanoholes have been published, obtaining sensitivities as high as  $0.9 \cdot 10^{-7}$  RIU, [16]. Transmittance by these nanostructures is considerably higher than in the case of circular nanoholes. Another important advantage is resolution. In the spectrum, sharper peaks are observed as light is highly polarized inside the holes.

Coupling plasmon to a Fabry-Perot cavity, where resonances are sharper than the corresponding to SPP, is a promising nanostructured system. In order to increase resolution and sensitivity, a microcavity of a dielectric material, usually glass, separates the bottom layer of the metallic corrugated thin film, where nanoholes are perforated, from another smooth thin film made of the same metallic material as the commented just before, as it can be observed in Figure 4.6 (a), [18]. Fabry-Perot resonances are found if the phase shift during a roundtrip by the wave is an integer multiple of  $2\pi$ . It must be considered that, due to nanoholes, an extra-shift will be found, more information about this topic is showed in section 5. When both resonances are matched, FWHM decreases considerably. This described configuration has been one of the most important objectives of this project, due to good resolution of this kind of devices.

Following the idea of Fabry-Perot resonances, a research group at Boston University has proposed a device, where flat metallic film commented before is substituted by nanodisks of the same diameter as nanoholes, see Figure 4.6 (b), [19]. In the obtained spectra, both kind of resonances can be perfectly distinguished. They demonstrated as Fabry-Perot resonances are even more sensible to changes in the refractive index than the corresponding to SPP.

Through the Babinet's principle, it is known that nanoholes and nanorods are equivalent. The last ones are usually set on a metallic medium. However, it has been proved as sensitivity increases significantly when a dielectric medium separates them from the flat film, Figure 4.6 (c), [20]. Also, signal-noise-ratio, increases, which is a very important advantage from an experimental point of view.

Recently, EOT has been achieved through a single sub-wavelength aperture. By the principle named previously, it is known that this kind of nanosystems show similar behaviors as nanoparticles, where localized surface plasmons are responsible for enhancement of the electric field in the nanoparticle surroundings, [21]. High intensity distribution in the nanoaperture rim is an important item in SERS (Surface Enhanced Raman Scattering) technique.

Light that emerges from a single aperture (nanoslit) is often unidirectional, which can be a problem in practical applications. Surrounding nanoaperture by a corrugated film, narrower beams are obtained, [22].

The confinement of surface plasmons polaritons at dielectric-metal interface in Terahertz regimen is really low. With the objective of increasing it, corrugated nanostructures have been proposed. Particularly, for exciting modes in two different spectral bands, devices where the height of grooves changes periodically have been manufactured, see Figure 4.6 (d), [23]. This means that nanogrooves height is repeated each two nanoholes.

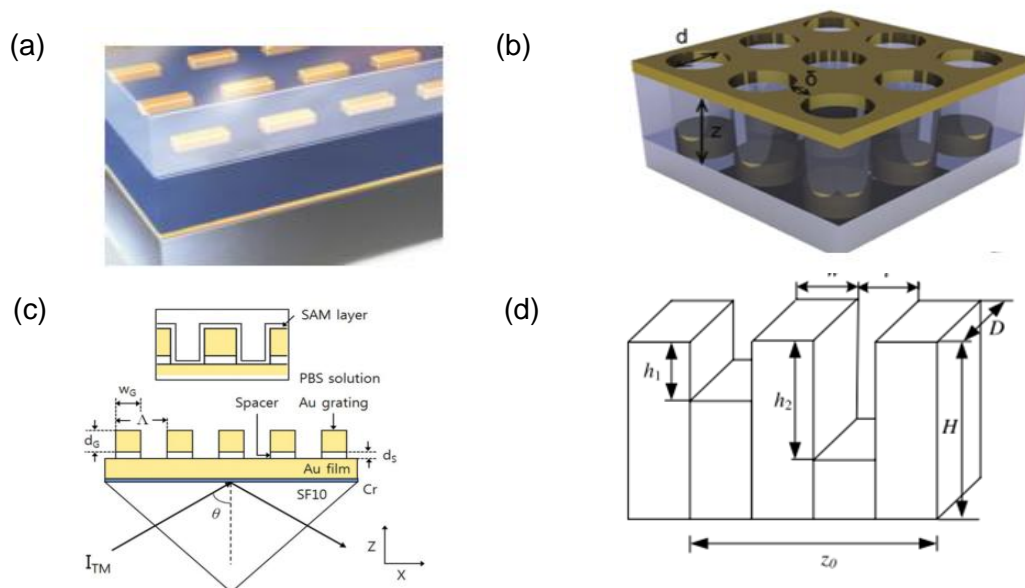


Figure 4.6: Schemes of some configurations described above. In (a) and (b) it is observed Fabry-Perot nanocavities. In (c) we can see a spacer between Au grating and Au film, which improves sensitivity. In (d) grooves of different height are shown.

## Fabry-Perot resonances

Fabry-Perot resonances are based on interferences with multiple waves. Configuration of a Fabry-Perot device consists of two plane-parallel plates opposite between them. An important feature of this kind of devices is that the inner faces of the layers are highly reflective. In spite of that fact, part of radiation is transmitted. These transmitted waves interfere. Constructive interference will be observed when the following condition is accomplished:

$$2d \cos \theta = k\lambda \quad (5.1)$$

where  $d$  is distance between both layers,  $k$  is an integer number and  $\theta$  is the incidence angle, as it can be observed in Figure 5.1. In this case it is supposed that the medium between layers is air. For different materials, expression 5.1 must be slightly modified, in order to take into account the medium refractive index ( $n$ ).

$$2nd \cos \theta = k\lambda \quad (5.2)$$

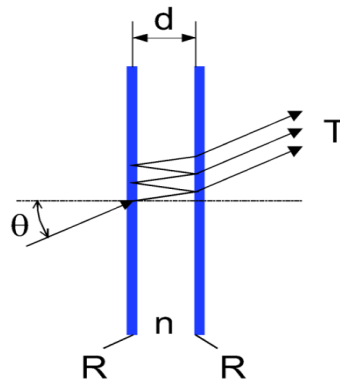


*Figure 5.1: Scheme of a Fabry-Perot cavity.*

Equations 5.1 and 5.2 are obtained taking into account that constructive interference is given when the optical path difference is an integer multiple of the impinging radiation wavelength. There is another common way of expressing equation 5.2, which makes reference to shift phase,  $\delta$  (constructive interference is gotten if  $\delta$  is an integer multiple of  $2\pi$ ), related with the optical path difference,  $\Delta$ , as:

$$\delta = \frac{2\pi}{\lambda} \Delta \quad (5.3)$$

As distance  $d$  increases, higher interferential orders will be observed and peaks will be sharper, which is a very important characteristic in resolution. Reflectivity is another factor that influences the width peaks, for the highest values of  $R$  we find the narrowest peaks.

Transmitted intensity corresponds with, [24]:

$$I = \frac{(1-R)^2}{(1-R)^2 + 4R \sin^2\left(\frac{\delta}{2}\right)} A_0^2 \quad (5.4)$$

being  $R$  reflectivity and  $A_0$  the amplitude of the incident radiation.

Through the Figure 5.2 it is observed as maxima of the transmitted intensity, represented as a function of the incident radiation wavelength, are not equispaced.

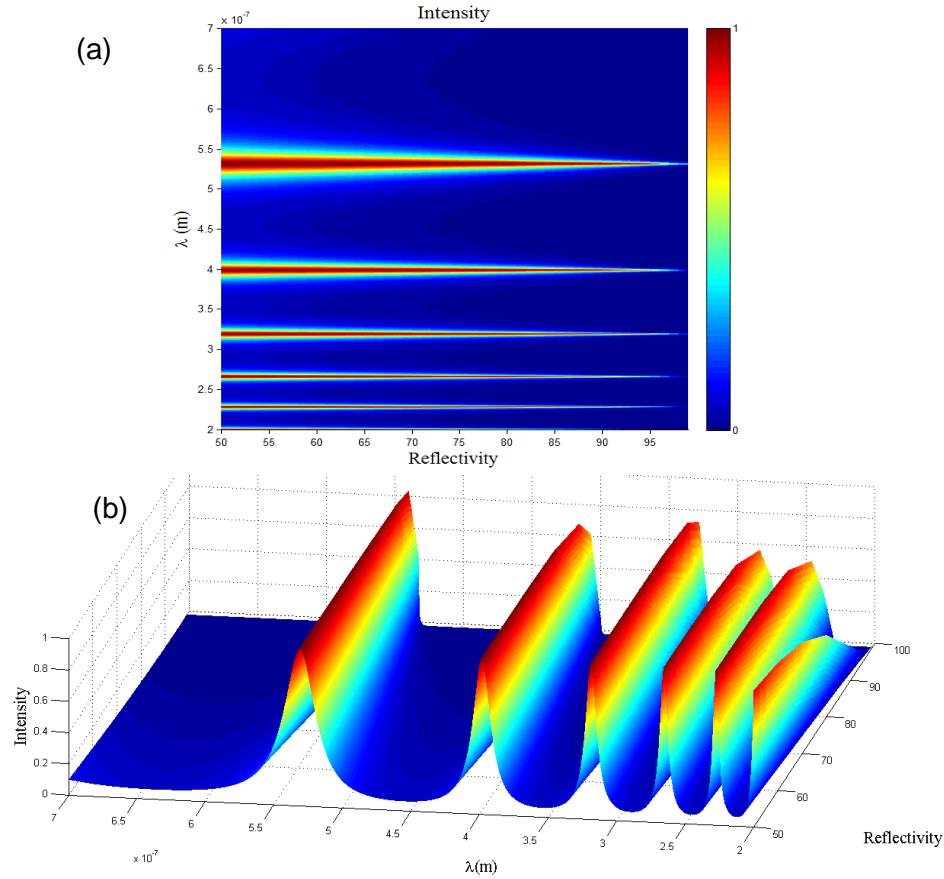


Figure 5.2: Transmitted intensity by a Fabry-Perot cavity as a function of the incident radiation wavelength and reflectivity.

In the project, we have simulated Fabry-Perot nanocavities. However, the shift phase is a little bit different to the commented before because one of the plates that constitute cavity is the base of the layer where nanoholes are perforated. So, the shift phase is the sum of three different contributions: the shift phase due to wave propagation in nanocavity, the corresponding to reflection in the bottom plate of the Fabry-Perot cavity and that due to the plasmon excitation in the nanostructured plate, [18].

$$\delta_{tot} = 2\delta_{prop} + \delta_{refl} + \delta_{exc} \quad (5.5)$$

Last term of equation 5.5 is given by the expression of a driven harmonic oscillator, [18]:

$$\delta_{exc} = \arctan\left(\frac{2\beta\omega}{\omega_{pl}^2 - \omega^2}\right) \quad (5.6)$$

$\beta$  represents the damping constant;  $\omega$  and  $\omega_{pl}$  are the frequency of the incident radiation and the plasmon resonance respectively.

Wood's anomalies were discovered by Wood in 1902, who was not able to give an explanation to so surprising phenomenon. Observing light spectra through gratings, he found how intensity suddenly decreased from maximum to minimum in a tiny range of wavelengths.

Rayleigh suggested that anomalies were observed to wavelengths where diffraction order changed to a higher one. In this case, the scattered wave is tangential to the grating surface. In order to know this wavelength theoretically, the following equation can be used, [25]:

$$\sin(\theta_n) = \sin(\theta) + \frac{n\lambda}{P} \quad (6.1)$$

where  $\theta$ ,  $\theta_n$  are the incident and diffracted angles respectively,  $\lambda$  is the wavelength of the incident radiation,  $P$  corresponds with the grating period and  $n$  is an integer number that makes reference to the diffraction order.

Taking into account that the diffraction order change is produced when  $\sin(\theta_n) = \pm 1$  and equation 6.1, it is possible to obtain wavelength where new diffraction order will be observed, [25]:

$$\lambda = \frac{(-\sin(\theta) \pm 1)P}{n} \quad (6.2)$$

Comparing theoretical and experimental results, it was observed a discrepancy of about 5%, which was explained by Rayleigh as an error in the grating period measurement. However, three decades later, Fano gave a convincing explanation to that disagreement between both results: two different kind of anomalies existed.

- Anomalies corresponding to the first kind, sharp anomalies, were observed to the wavelengths predicted by Rayleigh and governed by equation 6.2. Nowadays, they are known as Rayleigh anomalies.
- The second kind, [26], diffuse anomalies, extend in spectrum from the Rayleigh anomalies to a few more nanometers.

In this project, we have paid attention to the behavior of the Rayleigh anomaly.

The Rayleigh anomaly, at normal incidence, is observed when the diffracted wave is flush to the surface grating, most concretely, it is produced when the following equation is fulfilled, [27]:

$$\lambda_{RA} = \frac{P}{\sqrt{n^2 + m^2}} \sqrt{\epsilon_x} \quad (6.3)$$

where  $P$  is the period grating,  $n$  and  $m$  are integer numbers corresponding to different orders of the Rayleigh anomaly and  $\epsilon_x$  is the dielectric constant of the medium  $X$ .

In this project,  $\epsilon_x$  takes two different values corresponding to the dielectric constant of water,  $\epsilon_w$ , or glass,  $\epsilon_g$ . Due to this kind of devices are mainly used as biosensors, dielectric constant of buffer (water) is varied with the objective of obtaining the

sensitivity device. However, the glass dielectric constant value has remained constant to 2.25.

In spectra, we can observe Rayleigh anomalies and SPP, which are generated at the top of the metallic surface (water ( $n_i$ )-gold interface) or at the bottom (gold-glass ( $n_{iii}$ ) interface), see Figure 6.2.

From equations 4.2 and 6.3 it is possible to predict the peaks position and minima in spectrum. They correspond to SPP or RA, respectively. In Figure 6.3, it is represented the wavelength corresponding to SPP and RA peaks for (1,0) order as a function of the buffer refractive index. It must be noticed that on the right hand side of equations 4.2 and 6.3, the metal dielectric constant appears, which has been estimated using the Drude-Lorentz model, [28]:

$$\varepsilon(\omega) = \varepsilon_\infty - \frac{\omega_D^2}{\omega^2 + i\gamma_D\omega} - \sum_{m=1}^2 \frac{g_{Lm}\omega_{Lm}^2\Delta\varepsilon}{\omega^2 - \omega_{Lm}^2 + i2\gamma_{Lm}\omega} \quad (6.4)$$

where  $\varepsilon_\infty$  is the permittivity to infinite frequency,  $\omega$ ,  $\omega_D$  and  $\gamma_D$  are the incident radiation, the plasma frequency and the damping constant, according to Drude model,  $\omega_{Lm}$  and  $\gamma_{Lm}$  are the resonant frequency and the damping constant for the Lorentz model,  $g_{Lm}$  are the weights of  $\Delta\varepsilon$ , which are related with the oscillator strength. In the case of working with gold, the parameters named before take the following values:  $\varepsilon_\infty = 5.40$ ,  $\omega_D = 0.14 \cdot 10^{17} \text{ Hz}$ ,  $\gamma_D = 0.103 \cdot 10^{15} \text{ Hz}$ ,  $\omega_{L1} = 0.427 \cdot 10^{16} \text{ Hz}$ ,  $\omega_{L2} = 0.523 \cdot 10^{16} \text{ Hz}$ ,  $\gamma_{L1} = 0.870 \cdot 10^{15} \text{ Hz}$ ,  $\gamma_{L2} = 1.32 \cdot 10^{15} \text{ Hz}$ ,  $g_{L1} = 0.268$ ,  $g_{L2} = 0.732$  and  $\Delta\varepsilon = 2.54$ , [27].

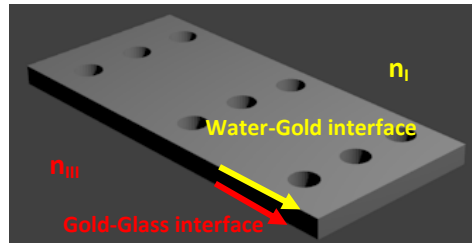


Figure 6.2: It is shown schematically the two surfaces where SPP and RA are generated.

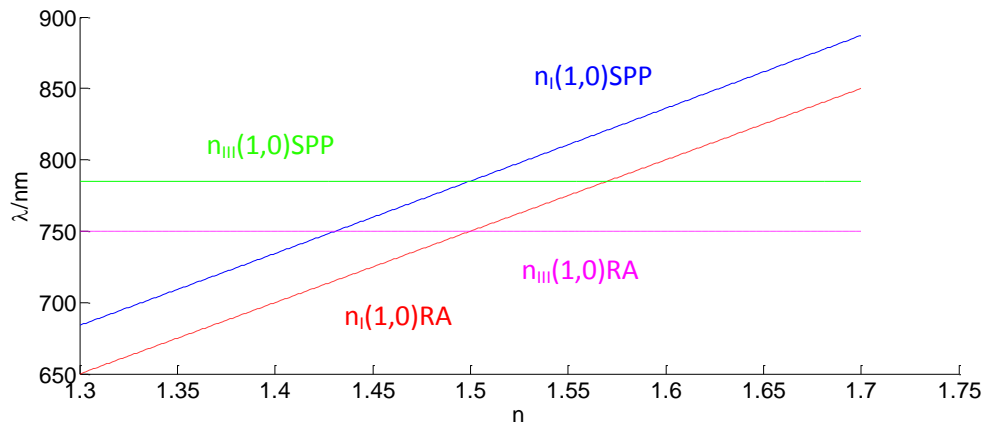


Figure 6.3: SPP and RA peaks position as a function of the buffer refractive index.

Accomplishment between SPP and RA at both interfaces provokes higher and narrower peaks in transmission spectra.

## Effective medium theory

For inhomogeneous media as the studied one in this project, where biological material is immersed in a buffer, generally water, the effective medium theory is applied. It is considered only one medium characterized by an effective refractive index which is related with the optics constants of the homogeneous buffer and the immersions. There are several theories concerning to this topic, each one of them is valid in a different range. It is considered that Maxwell Garnett is one of the most popular, [29].

The dielectric function for a medium with spherical inclusions, according to Maxwell Garnett theory, is given by the following expression:

$$\varepsilon_{av} = \varepsilon_m \left[ 1 + \frac{3f \left( \frac{\varepsilon - \varepsilon_m}{\varepsilon + 2\varepsilon_m} \right)}{1 - f \left( \frac{\varepsilon - \varepsilon_m}{\varepsilon + 2\varepsilon_m} \right)} \right] \quad (7.1)$$

where  $\varepsilon_m$ ,  $\varepsilon$  are the buffer and immersions dielectric constants, respectively, and  $f$  corresponds to the inclusions volume respect to the total volume.

In case of Bruggeman theory, dielectric constant function is:

$$f \frac{\varepsilon - \varepsilon_{av}}{\varepsilon + 2\varepsilon_{av}} + (1 - f) \frac{\varepsilon_m - \varepsilon_{av}}{\varepsilon_m + 2\varepsilon_{av}} = 0 \quad (7.2)$$

$\varepsilon_{av}$  represents the medium average dielectric constant.

Although equations 7.1 and 7.2 come from a common expression, in order to obtain them, different approaches must be done. So, its validation is different depending on the considered problem. The most important difference between both theories consists of the second one considers a mixture of two different homogeneous media, without distinguishing between matrix and inclusions as in the first one.

In general, problem cannot be solved in an analytical way. So, it is necessary to resort to numerical methods. In this project, we have used the commercial software: COMSOL, which is based on the Finite Element Method (FEM).

This program is able to solve partial differential equations in an efficient way. For this reason, it is really useful in different aspects of physics and engineering, [30].

Although this software is made up of several modules, we have paid attention to the electromagnetic one, which allows solving this kind of problems.

First of all, it is necessary to build geometry, Figure 8.1 and specify materials which different parts of the structure are made of. Respect to illumination, different kind of incident radiation can be introduced: a plane wave, a Gaussian beam...., see Figure 8.2, in all cases, choosing the polarization and the propagation direction of the impinging light.

In order to solve the problem, it must be discretized in several points, where, in each one of them, Maxwell equations are worked out. Consequently, number of elements that compose the mesh must be enough big for having accurate results.

For simulating an infinite structure, due to problem complexity, only a unit cell is created and Floquet periodicity conditions are applied in both transversal directions to the propagation direction, as it can be observed in Figure 8.1. Through COMSOL, reflection and transmission spectra and near field images are obtained by a direct way, [31], [32].

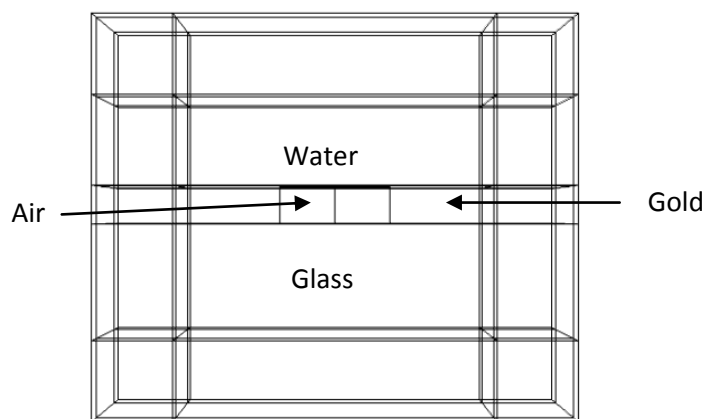


Figure 8.1: Unit cell, which is repeated periodically, created with COMSOL.

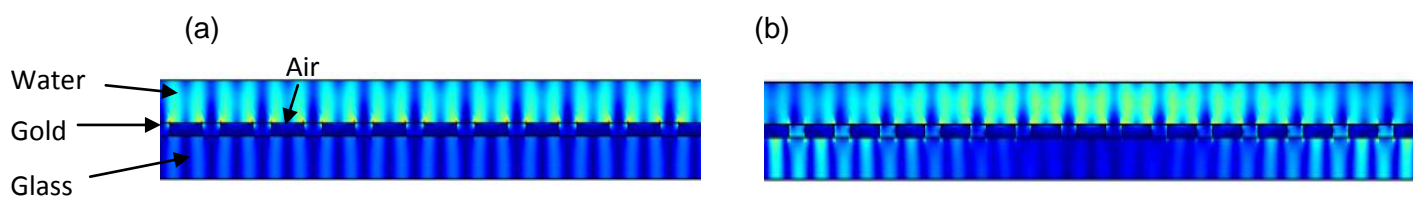


Figure 8.2: Near field images of a grating structure in 2-D when it is illuminated with (a) a plane wave, (b) a Gaussian beam.

Knowledge of interaction between electromagnetic radiation and matter to nanoscale has advanced in the last decades due to two main factors: development of numerical methods and nanotechnology. Thanks to these two aspects, physical phenomena as extraordinary optical transmission (EOT) can be explained and observed in real devices.

Due to the high sensitivity to tiny variations in the buffer refractive index, generated as a consequence of immersions of different materials (essentially biological) with a refractive index slightly higher than the corresponding to the buffer, the most important applications of EOT are found in medicine, biology and SERS technique.

### 9.1 Medicine and biology

In order to detect biological material in low concentrations, biosensors based on EOT have been manufactured. However, much effort is necessary to develop biosensors with higher sensitivities. Another point to take into account is the feasibility of carrying out these devices experimentally. All of them present a common structure, which consists of nanoholes perforated in thin metallic films set on a dielectric substrate, generally, quartz (glass). On the dispositive is set the sample to study. In literature there are several examples of biosensors that are able to detect different materials: proteins [8], cancer cells [33]...

Changes in the refractive index are put in evidence in spectra by spectral shifts.

### 9.2 Surface-enhanced Raman Scattering

It is a spectroscopy technique based on the Raman Effect. It is based on the amplification of the vibrational spectrum of molecules that are settled onto the nanostructured metallic surface. It is vastly used for detecting biological material in low concentrations.

Due to the enhancement of the electric field produced in nanoholes surrounding as a consequence of surface plasmons, Raman scattering is enhanced. For this reason, nanohole arrays, where surface plasmons are present, are so interesting in this spectroscopy technique, [34].

### 9.3 Another interesting applications

- Surface-enhanced fluorescence: it allows detecting biological species which are 5 nm away from surface due to surface plasmon field, [34].
- Polarization control: it can be controlled by nanohole shape, getting nanopolarizers, [34].
- Non linear effects: they can be enhanced by the presence of nanohole arrays, [34].

In this section we show the main studied configurations with their transmission/reflection spectra and their sensitivity to changes in the buffer refractive index. We analyze the advantages and disadvantages of each simulated biosensor.

Due to computational problems associated to simulate biologic material in 3-D (lack of memory and computational time), we decided to use the effective medium theory in order to carry out all the results obtained for the different biosensors.

Before analyzing all the simulated biosensors, in section 10.1 we study the validity of the effective medium theory for our problem, studying the change in the refractive index buffer, water  $n_w=1.33$ , due to introduction of material with a slightly higher refractive index,  $n_m=1.40$ .

According to the results obtained in section 10.1, in the following sections we have worked with an effective refractive index, which has changed from 1.330 to 1.340 with steps of 0.002, studying the sensitivity of the simulated biosensors. In order to achieve high sensitivities, different geometries have been analyzed.

For all the cases we have simulated a gold nanohole array, set on a dielectric substrate. The nanohole diameter and the period correspond with 180 and 500nm respectively. The numerical method used was COMSOL.

### 10.1 Validation of effective medium theory

Due to enormous dimensions, around microns, simulating biologic material on a biosensor is almost impossible from a computational point of view, number of elements that composes the mesh is too much big. For this reason, we decided to modelize the problem to solve in 2-D. In all the cases biosensor was illuminated with a Gaussian beam, polarized in x-axis and propagating in  $-y$ , normal incidence, which is given by the following expression:

$$\vec{E} = E_{0x} \frac{\omega_0}{\omega(y)} e^{-\left(\frac{r}{\omega(y)}\right)^2} \cos(\omega t - ky + \eta(y) - r^2 \frac{k}{2R(y)}) \quad (10.1)$$

where  $r = \sqrt{x^2}$ ,  $E_{0x}$  is the amplitude of the electric field in x-direction,  $k$  is the wave number,  $\omega$  is the angular frequency, and  $\omega(y)$ ,  $\eta(y)$  and  $R(y)$  are expressed as:

$$\omega(y) = \omega_0 \sqrt{1 + \frac{y}{y_0}} \quad \eta(y) = \text{atan}\left(\frac{y}{y_0}\right) \quad R(y) = y \left(1 + \left(\frac{y_0}{y}\right)^2\right) \quad (10.2)$$

being  $\omega_0$  the minimum waist beam and  $y_0$  is related with  $\omega_0$  by:  $y_0 = \frac{\pi \omega_0^2}{\lambda}$

In the analyzed cases  $\omega_0$  corresponds to 20 $\mu\text{m}$ .

Simulation consists of a thin gold film, whose thickness is 60nm, where nanoholes have been perforated. They present rectangular shape of dimensions 60X180nm and

are filled of air. Period, distance between two consecutive holes, corresponds to  $P=500\text{nm}$ . Metallic film is set on a dielectric substrate, glass. On nanohole grating, we set a rectangular material, whose area is  $0.12\mu\text{m}^2$  ( $100\times 1200\text{nm}$ ) and refractive index is 1.40, which is immersed in a liquid buffer, in this case, water.

A scheme of the studied geometry is shown in the following Figure, 10.1:

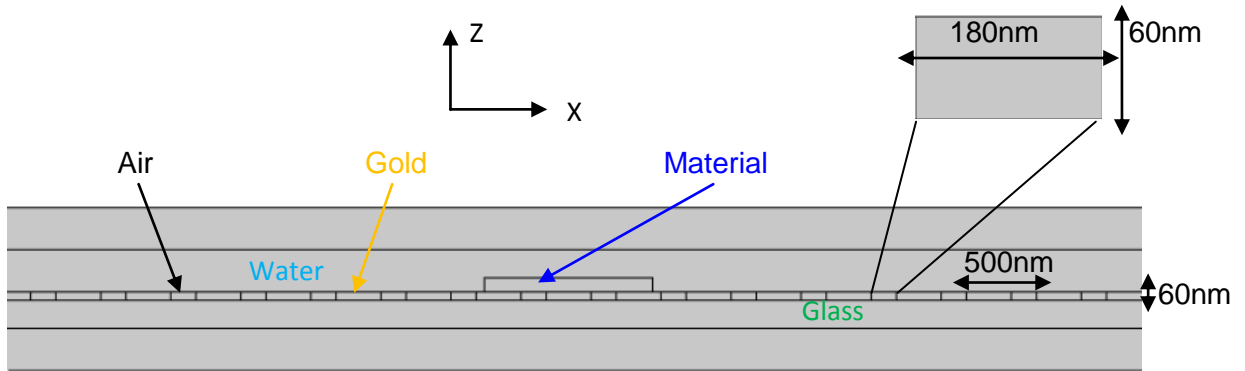


Figure 10.1: Scheme of the modeled biosensor, where it can be observed the material introduced in the buffer.

First of all, we have studied transmission spectrum by a structure like the shown in Figure 10.1 but taking away the material that is above the grating. The result obtained is observed in Figure 10.2.

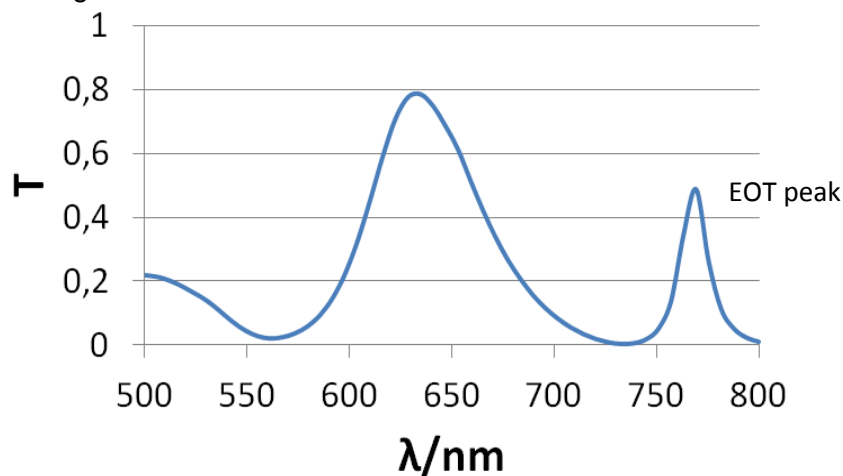
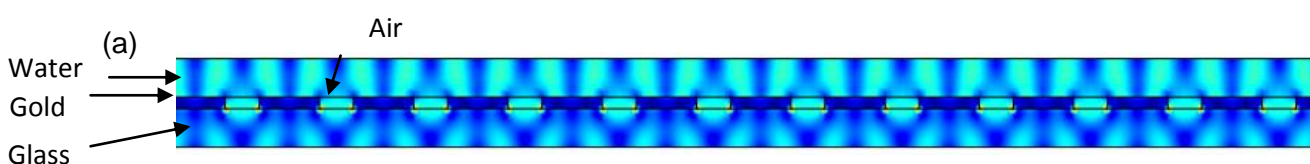


Figure 10.2: Zero-order transmission of Au film at normal incidence,  $P=500\text{nm}$ ,  $t=60\text{nm}$ ,  $d=180\text{nm}$ .

Peaks shown in spectrum, from left to right side, are due to Wood's anomalies and extraordinary optical transmission respectively. Near field maps corresponding to both of them can be observed in Figure 10.3.



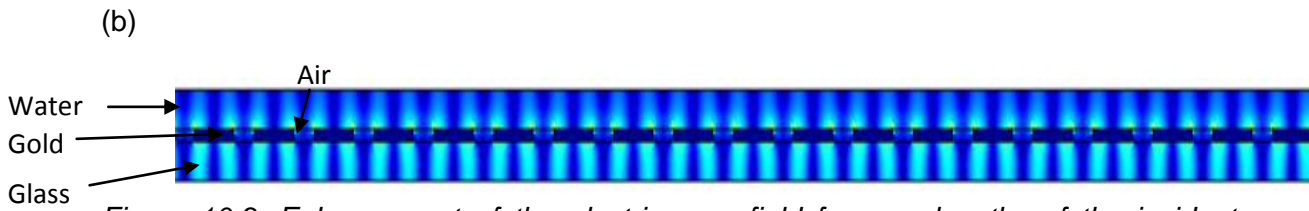


Figure 10.3: Enhancement of the electric near field for wavelengths of the incident radiation corresponding to the observed resonances (a) Wood anomaly (634nm) and (b) EOT peak (769nm).

For studying sensitivity of this structure to changes in the refractive index, we have varied the buffer refractive index from 1.330 to 1.340 each 0.002, paying attention to the spectral region corresponding to the EOT peak, see Figure 10.4.

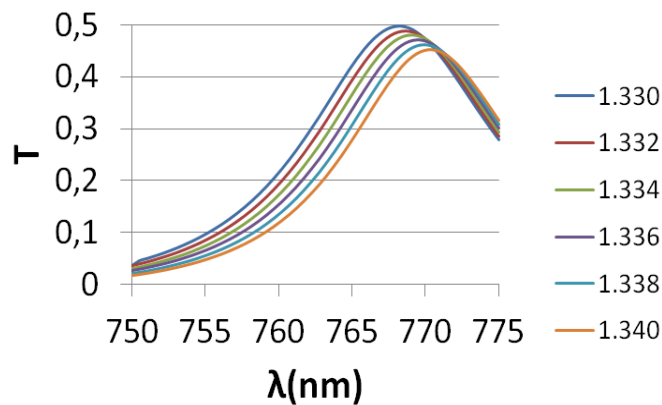


Figure 10.4: Zero-order transmission of Au film at normal incidence,  $P=500\text{nm}$ ,  $t=60\text{nm}$ ,  $d=180\text{nm}$ , paying attention to the spectral regions between 750-775nm, EOT peak.

Representing the maxima values of the EOT peak as a function of the refractive index, it is possible to obtain the sensitivity: 230nm/RIU, see Figure 10.5.

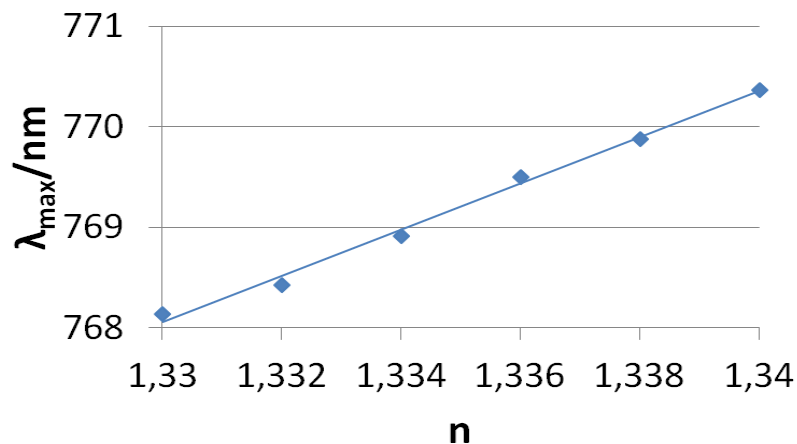


Figure 10.5: It is shown the wavelength where maximum in transmission spectrum of Figure 10.4 is found, as a function of the refractive index.

In order to know the effect of immersions, we have supposed that material, whose refractive index is 1.4, fills a 3% of the buffer area (1.33), which according to the effective medium theory supposes a change in the buffer refractive index

corresponding to 0.002. All immersions have an area of  $0.12 \mu\text{m}^2$ , and its number has changed from 1 to 5, see Figure 10.6.

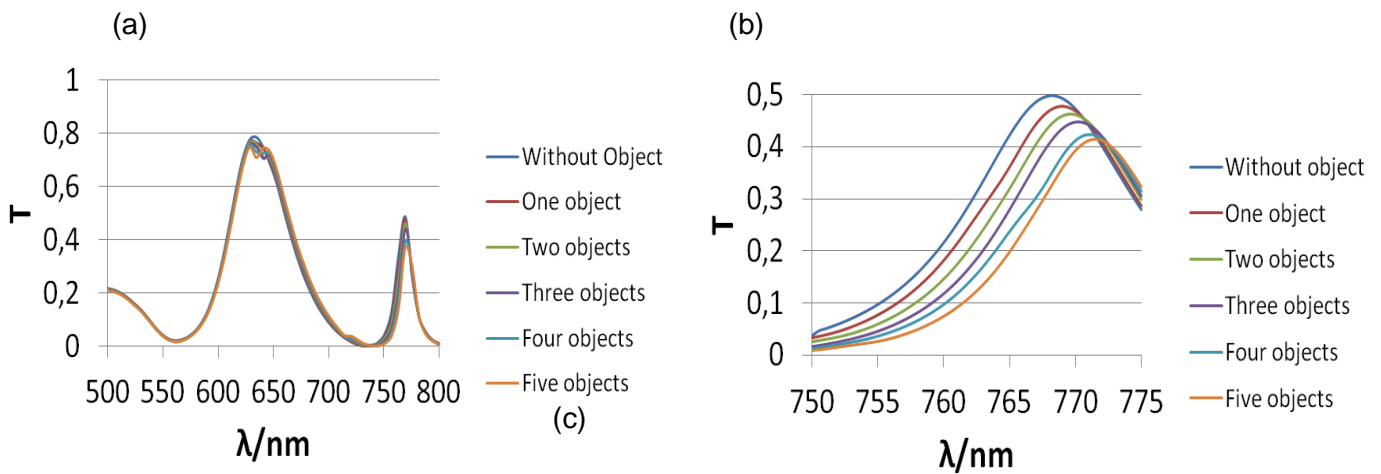


Figure 10.6: Zero-order transmission of Au film at normal incidence,  $P=500\text{nm}$ ,  $t=60\text{nm}$ ,  $d=180\text{nm}$ , as a function of number of objects (area  $0.12 \mu\text{m}^2$ ) with refractive index 1.40, immersed in water for the ranges between (a) 500-800nm, (b) 750-775nm.

As number of objects increases, transmission diminishes and a red-shift of peaks is observed due to light goes through an optically denser medium.

In Figure 10.7 near field maps can be observed for the two resonances shown in spectrum exhibited in Figure 10.6 (a) when an only object is immersed in the buffer.

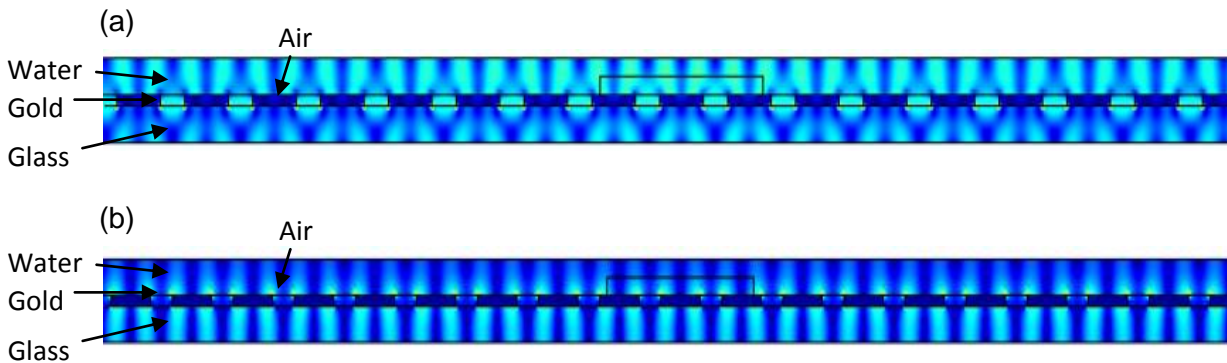


Figure 10.7: Near field maps corresponding to the following wavelengths: (a) 634nm and (b) 769nm.

Transmission spectra, obtained by introducing material with a higher refractive index than the corresponding to the buffer, have been compared with those gotten applying the effective medium theory. The found results are shown in Figure 10.8.

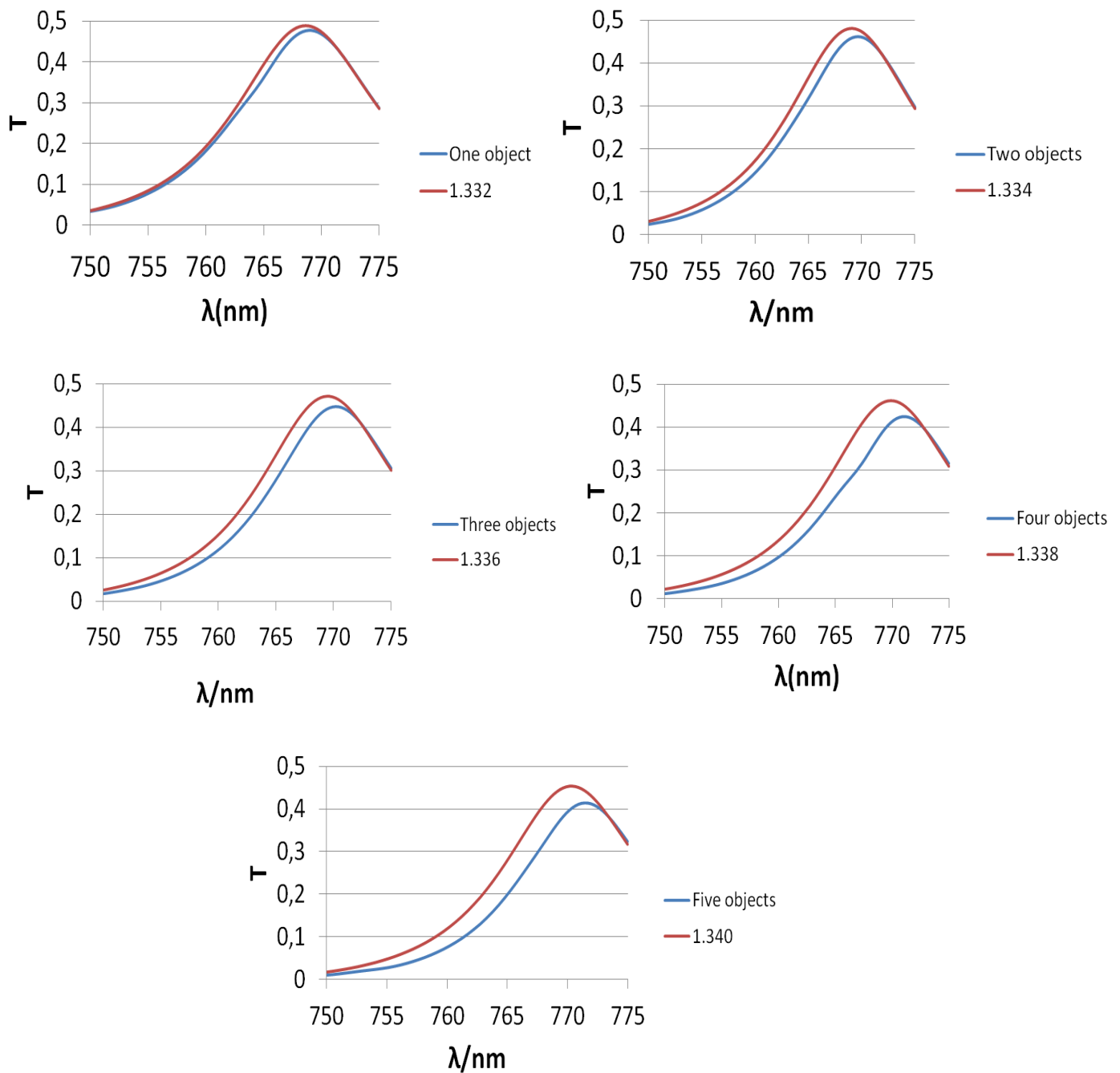


Figure 10.8: Comparison between transmission spectra considering buffer ( $n_w=1.33$ ) with different number of immersions ( $n_m=1.40$ ) and effective medium theory.

We observe that the behavior of transmission spectra changing the buffer refractive index and the number of immersions is similar. Also, for a number of objects lower than three, we observe that matching between both graphs is almost perfect. However, for a number of objects greater than three, the spectral shift corresponding to change the number of objects is bigger than the corresponding to change the buffer refractive index. For this reason, we have concluded that applying the effective medium theory supposes a lower bound in the sensitivity results obtained.

## 10.2 Sensitivity in different geometries

In the section before, it was proved as effective medium theory is useful in order to simulate biologic material in a biosensor, so that, we decided to use it in simulations carried out in this part.

These systems are able to detect low variations in the buffer refractive index, for this reason, they are used as biosensors.

### 10.2.1 Basic device. Thin film with nanoholes

For simulating an infinite structure in COMSOL it is necessary to build a unit cell and establishing periodic conditions in both cell sides. In this configuration a thin metallic film (gold, thickness  $t=60\text{nm}$ ), is deposited on a dielectric substrate, glass  $n_g=1.5$ , as it can be observed in Figure 10.9. On nanohole array, we find the liquid buffer, water  $n_w=1.33$ . Nanoholes, whose diameter is  $180\text{nm}$ , are filled of air. Period is  $500\text{nm}$ . Illumination consists on a plane wave polarized in x-axis, which propagates in  $-z$ -axis.

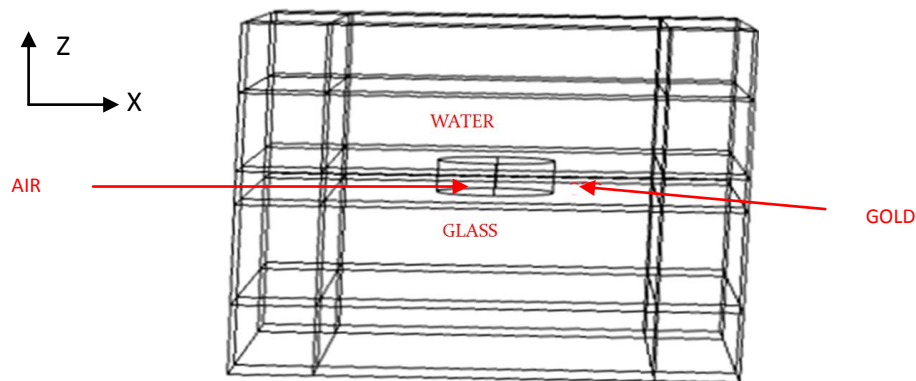


Figure 10.9: Unit cell of the simulated structure.

For this structure we have obtained the transmission spectrum, shown in Figure 10.10:

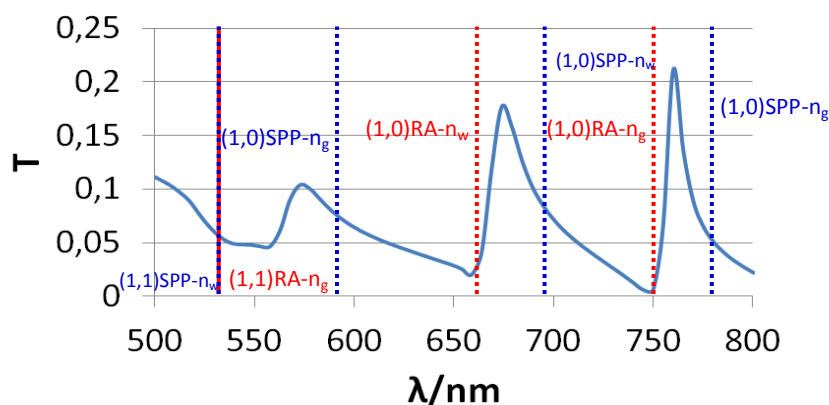


Figure 10.10: Zero-order transmission of Au film at normal incidence,  $P=500\text{nm}$ ,  $t=60\text{nm}$ ,  $d=180\text{nm}$ .

Comparing Figures 10.2 and 10.10 it is observed as peaks that appear in spectra are different, as it was hoped, due to interactions in a 2-D nanohole array are not the same

as in a 3-D nanostructure. In the case of 3-D simulations we can see three EOT different peaks, while in the 2-D spectrum we only observed an only EOT peak. Taking into account expressions 4.1 and 6.3 we have identified the different contributions that appear in spectrum, which have been marked in the Figure 10.10. Minima in spectra are given at wavelengths where Rayleigh anomalies take place. Maxima correspond to surface plasmons at dielectric-metal interfaces, although they appear blue-shifted respect to the theoretical positions, see section 6, Figure 6.3. This spectral shift is mostly due to different dielectric constants used in the analytical study (Drude-Lorentz model, [27]) and numerical (Palik's handbook, [15]) results, and to accomplishment between surface plasmons of both metallic-dielectric interfaces, the corresponding to water-gold and gold-glass.

We paid attention to the peak on the right, the most intense one, with the objective of varying the buffer refractive index and obtaining the sensitivity, see Figure 10.11.

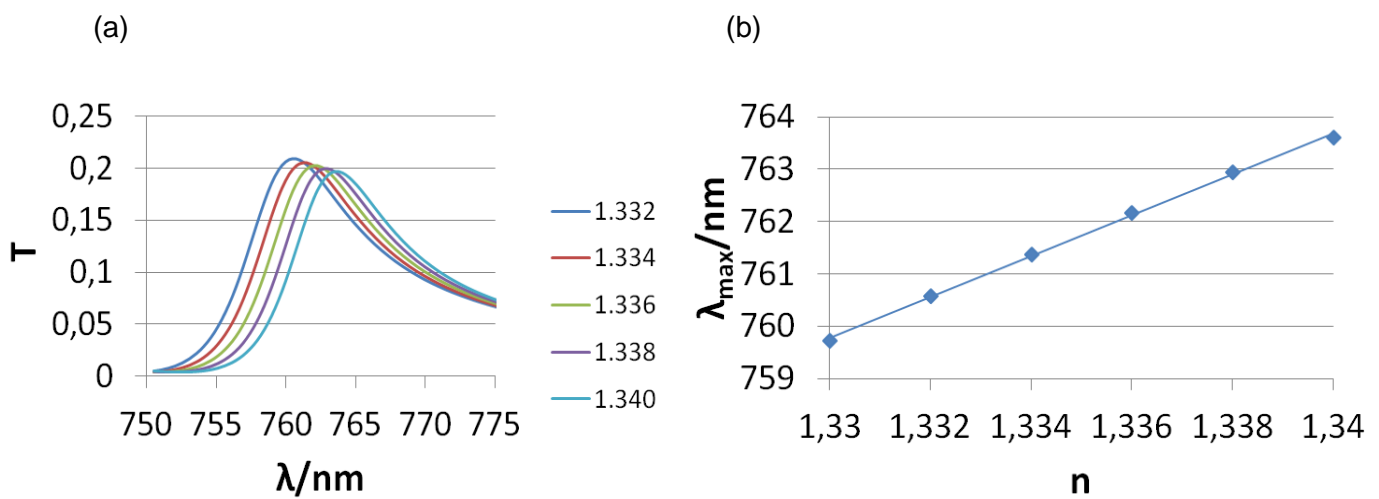


Figure 10.11: (a) Transmission spectra for different refractive indexes of the considered buffer. (b) Sensitivity curve for the configuration shown in the Figure 10.9.

By the slope of the Figure 10.11 (b) it is obtained a sensitivity of 390.71nm/RIU, which is almost double that the value gotten for 2-D calculations.

In near field, EOT phenomenon is manifested by an enhancement of the electric field in the surroundings of nanoholes, see Figure 10.12.

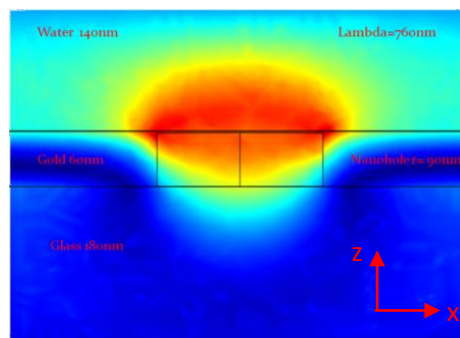


Figure 10.12: Near field map of the simulated unit cell when it is illuminated with a plane wave of 760nm, polarized in x-axis and propagating in  $-z$ -axis.

Illuminating an infinite structure with a plane wave is equivalent to light infinite nanoholes, which does not correspond with a real situation. In order to solve this problem, we decided to use a Gaussian beam. Transmission spectra acquired for different spot sizes are shown in the following Figure, 10.13:

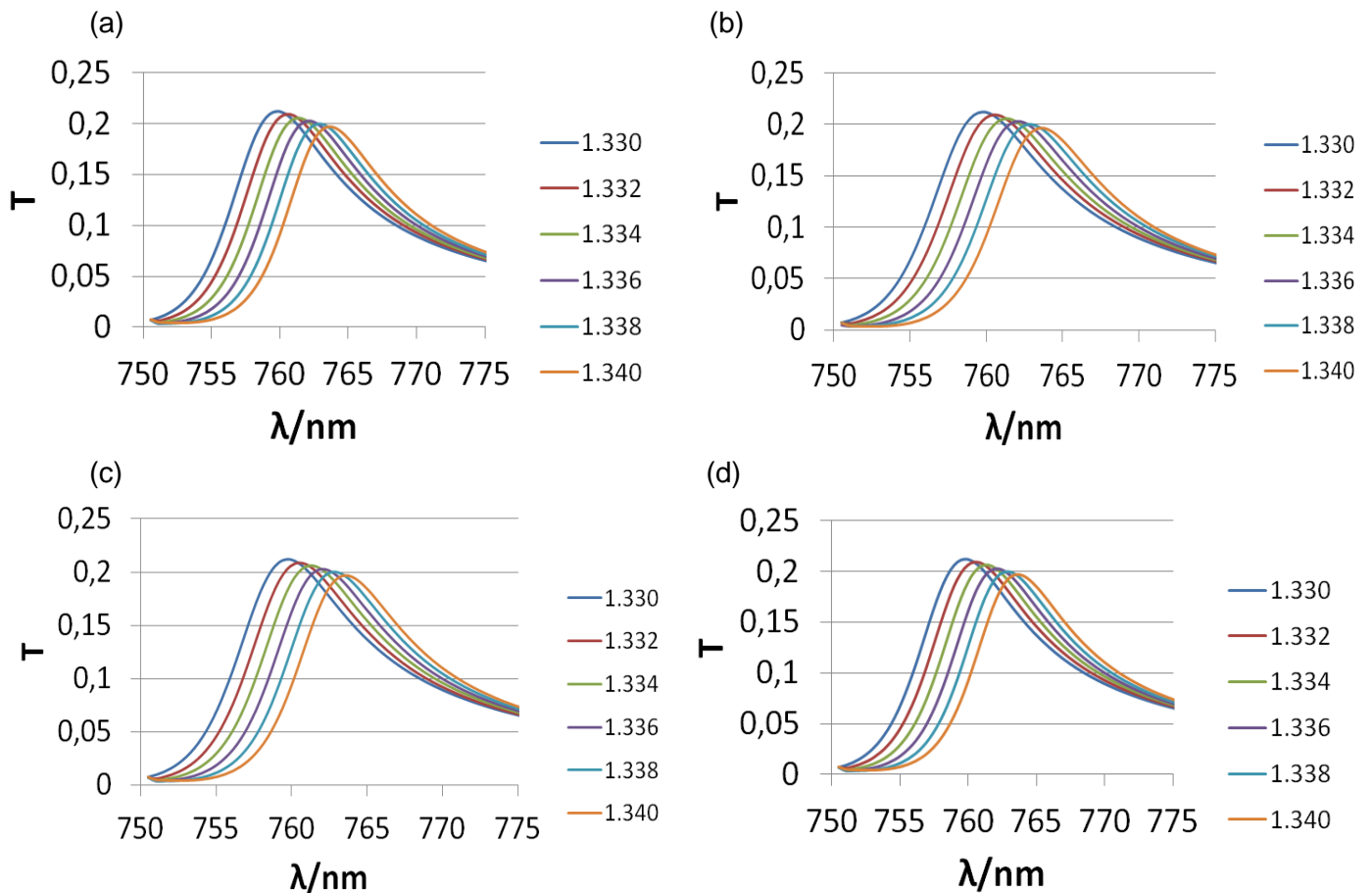


Figure 10.13: Transmission spectra obtained by illuminating the nanostructure with a Gaussian beam for the spot sizes: (a)  $25\mu\text{m}$ , (b)  $20\mu\text{m}$ , (c)  $10\mu\text{m}$ , (d)  $5\mu\text{m}$ .

For the spots studied: 25, 20, 10,  $5\mu\text{m}$ , number of illuminated nanoholes corresponds with 2500, 1600, 400, 100, respectively. In all cases the spectrum obtained is identical to the exhibited by a periodic structure. This means that illuminating infinite holes is equivalent to light a big amount of them. For this reason, in the rest of the project we decided to simulate plane waves, which is a little bit easier.

With the objective of increasing sensitivity and designing a device, which can be manufactured in an easy way, we decided to study different structures. Some of them are shown in the following pages.

### 10.2.2 Thin film with nanoholes and cavity effects I

In the next studied geometry, under the glass substrate of Figure 10.9, we built a gold film of thickness 300nm (to a distance of 380nm from the nanohole array) and another glass layer, see Figure 10.17. The illumination is the same as the commented for the above geometry, and it will be the same for the rest of the studied configurations.

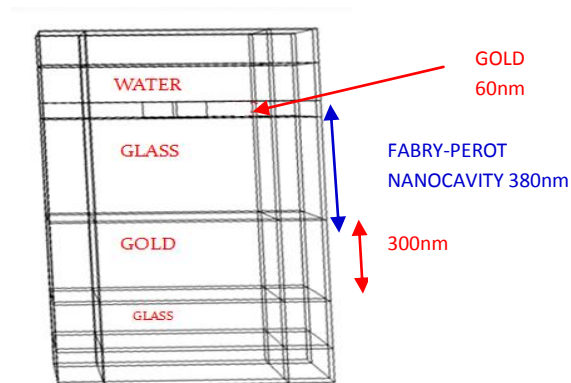


Figure 10.14: Unit cell of the configuration described just before, where a Fabry-Perot nanocavity has been incorporated.

We decided to study reflection instead of transmission due to this last one is really low as a consequence of absorption in the metal layer, gold 300nm, Figure 10.14.

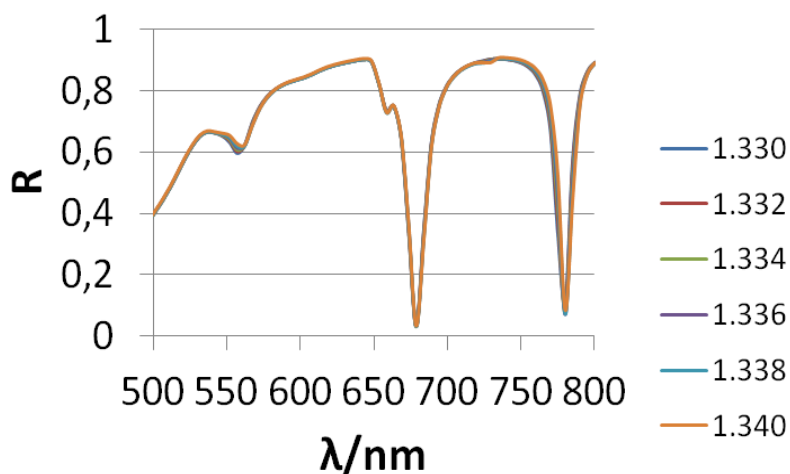


Figure 10.15: Reflection spectrum for the structure specified in Figure 10.14.

Peak observed to 780.5nm is due to EOT while the corresponding to 679.2nm is a Fabry-Perot resonance, which, due to buffer location is not sensible to changes in water refractive index. So, for studying sensitivity of this device, we paid attention to the peak on the right side, Figure 10.16.

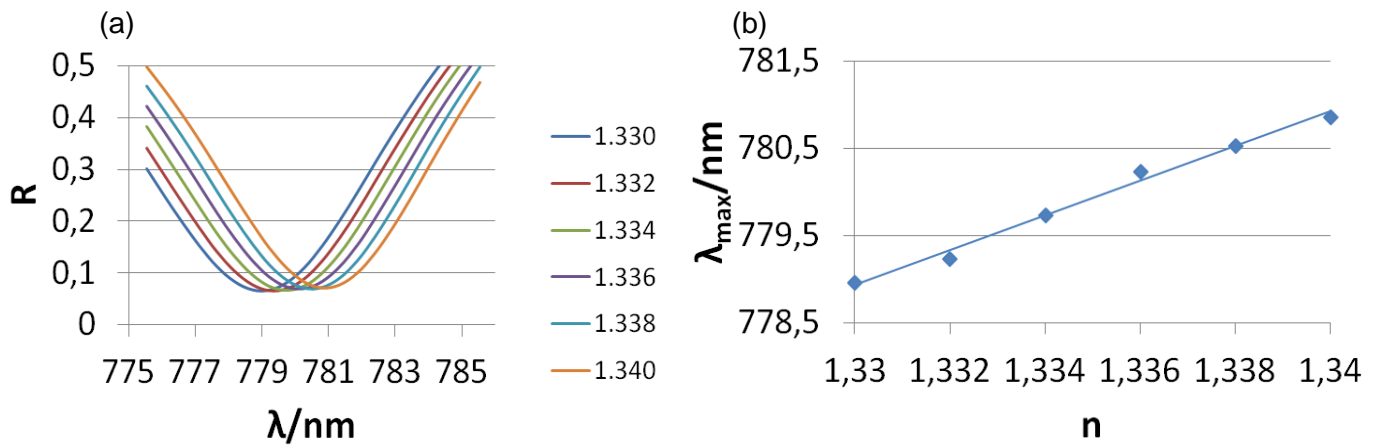


Figure 10.16: (a) Reflection spectra for different refractive indexes of the buffer, from 1.330 to 1.340 with steps of 0.002. (b) Sensitivity curve.

Sensitivity obtained for this nanostructure corresponds with 198.6nm/RIU. It is lower than the gotten for the first considered structure (just one layer with nanoholes). However, from an experimental point of view, this geometry presents two important advantages: it is easier to detect minima in intensity of light than maxima, and peaks are narrower.

With the objective of observing Fabry-Perot resonances in transmission spectra, we simulated an identical geometry to the shown in Figure 10.14 but where gold layer thickness was 20 instead of 300nm, see Figures 10.17 and 10.18.

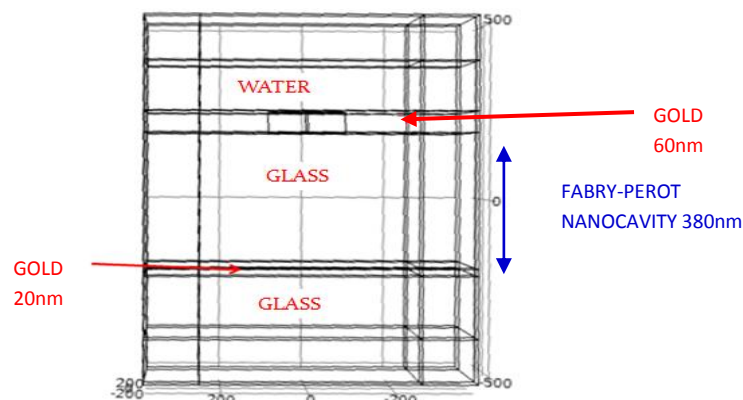


Figure 10.17: Scheme of the studied geometry.

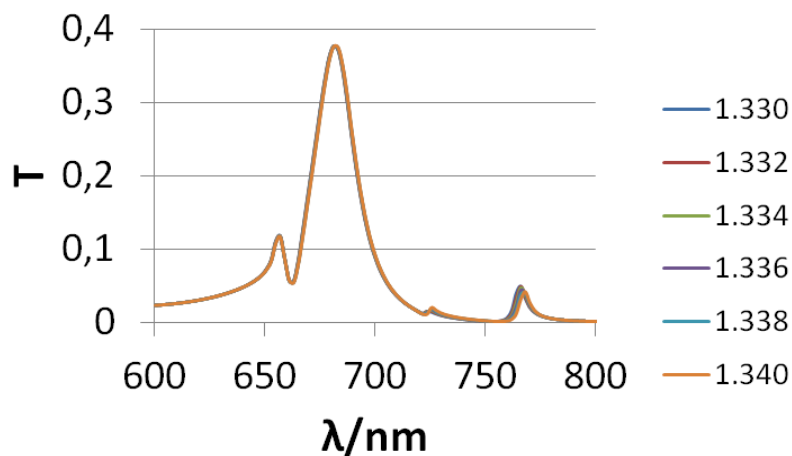


Figure 10.18: Transmission spectrum for the configuration shown in Figure 10.17.

Through the above spectrum we can observe two remarkable peaks, the one set on the right side is due to EOT, and the corresponding to 681.6nm (the highest peak) is a Fabry-Perot resonance. We have analyzed each one of these peaks in an independent way, Figure 10.22.

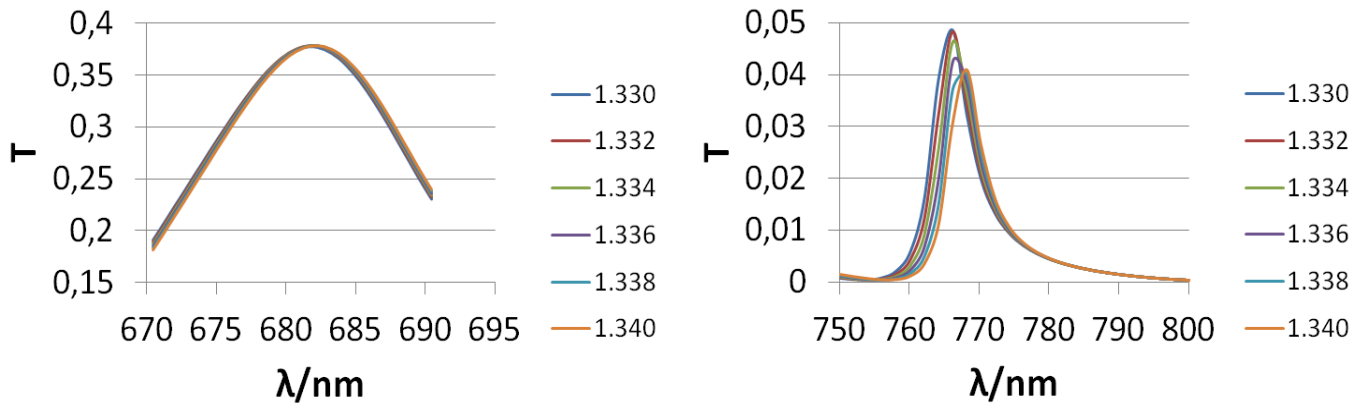


Figure 10.19: It is shown transmission for the spectral regions corresponding to the most remarkable peaks observed in Figure 10.18.

In the Figure on the left, we can see as the peak position remains constant although the buffer refractive index changes. This observed behavior is due to this peak corresponds to a Fabry-Perot resonance in the glass nanocavity, where refractive index is  $n_g=1.5$ , so that, it is not sensible to changes in the water refractive index. However, in the spectrum on the right, it is shown a spectral shift because that peak is a consequence of the EOT phenomenon, which, according to equation 4.2, depending on the buffer refractive index, the peak will be observed to different wavelengths.

This configuration is not optimum due to the wavelength, where the Fabry-Perot resonance appears, is constant and the EOT peak takes values really low.

### 10.2.3 Thin film with nanoholes and cavity effects II

In order to obtain changes in the transmission peak corresponding to the Fabry-Perot resonance, we decided to simulate a structure as the presented in the Figure 10.17 but, where the buffer is introduced in the Fabry-Perot nanocavity and the glass substrate is set on the nanohole array, see Figure 10.20.

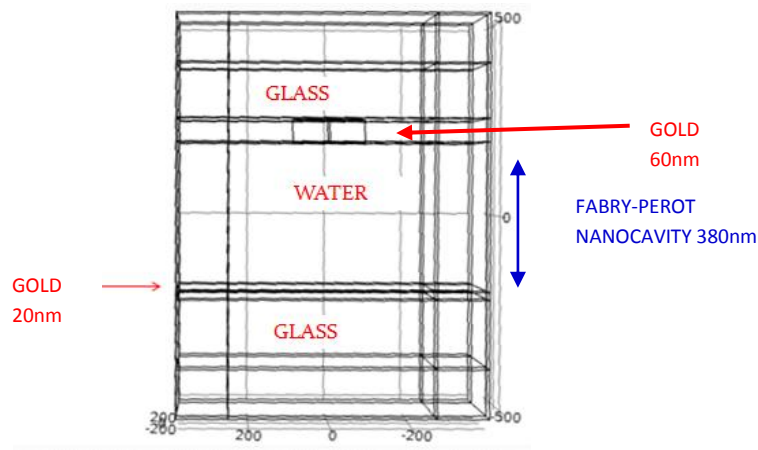


Figure 10.20: It is observed that the buffer, water, is introduced in the Fabry-Perot nanocavity.

The transmission spectrum obtained in this case, can be observed in the Figure 10.21.

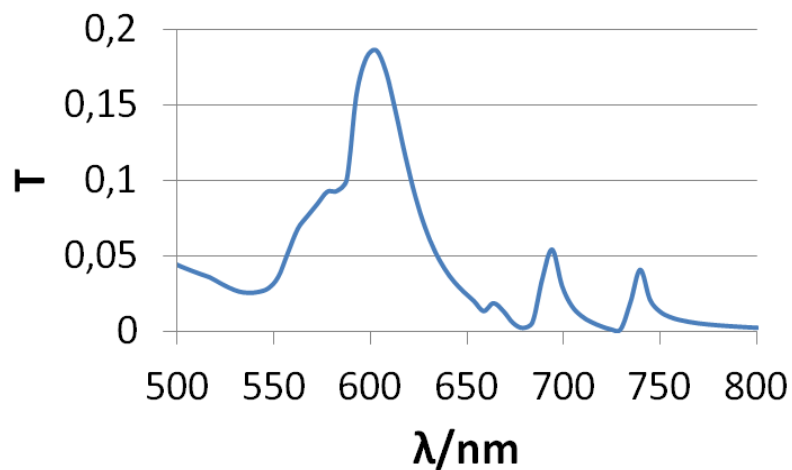


Figure 10.21: Transmission spectrum for the configuration shown in the Figure 10.20.

We have paid attention to the highest peak, corresponding to a Fabry-Perot resonance. Changing the buffer refractive index we have obtained the sensitivity for this nanostructure, Figure 10.22.

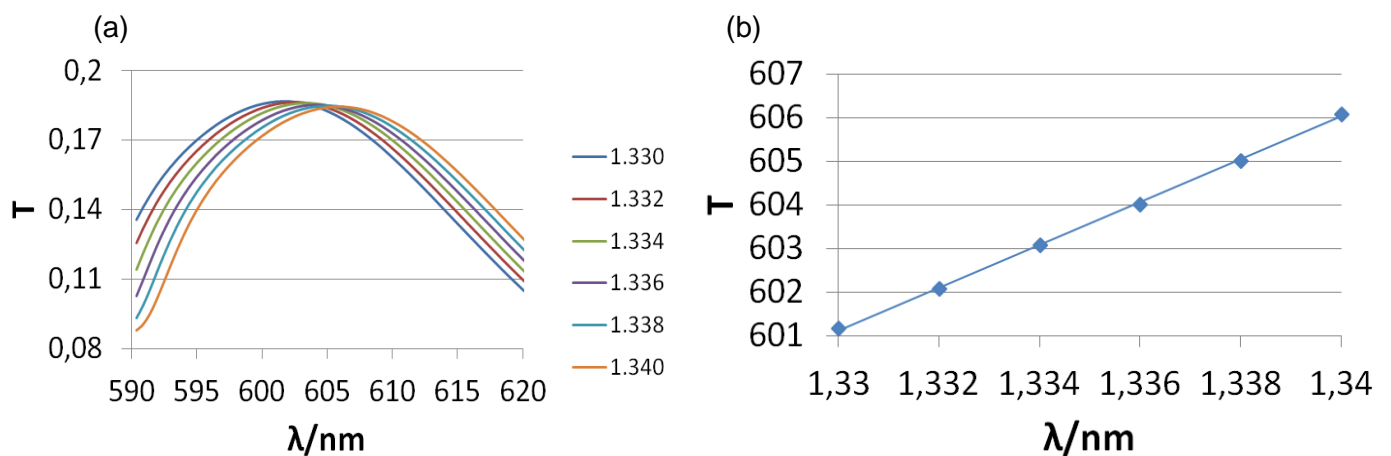


Figure 10.22: (a) Spectral shift of the Fabry-Perot resonance, (b) sensitivity.

The sensitivity obtained corresponds with 489.72nm/RIU, which is high. So, theoretically, this configuration could be promising as biosensor. However, it is difficult to manufacture due to the necessary microfluidic for introducing the buffer through the Fabry-Perot nano/micro cavity.

Observing the transmission peaks, it is clear that they reach low values (see Figure 10.21). For increasing the transmission, we decided to fix the thickness of the gold thin film where nanoholes are perforated to 20nm instead of 60nm like in the previous cases. When the thickness of the gold film decreases, transmission increases, because of the lower absorption.

The simulated geometry can be observed in the Figure 10.23:

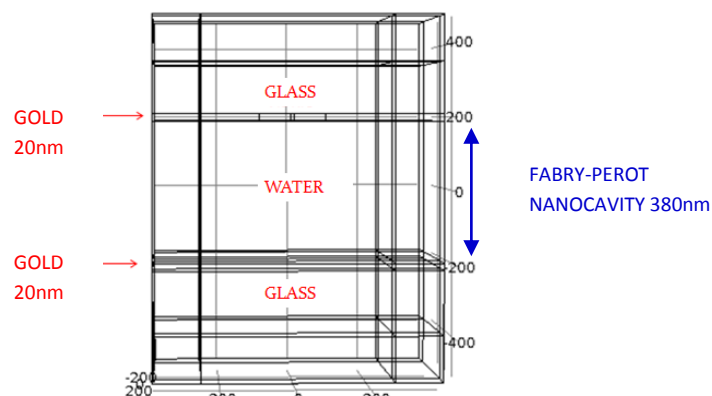


Figure 10.23: Scheme of the described geometry.

The transmission spectrum is observed in the Figure 10.24:

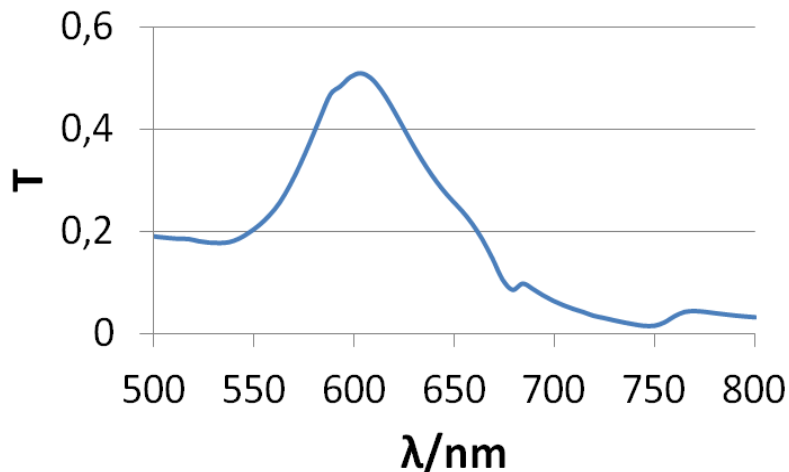


Figure 10.24: Transmission spectrum for the configuration exhibited in the Figure 10.23.

Varying the buffer refractive index we obtain the results shown in the Figure 10.25:

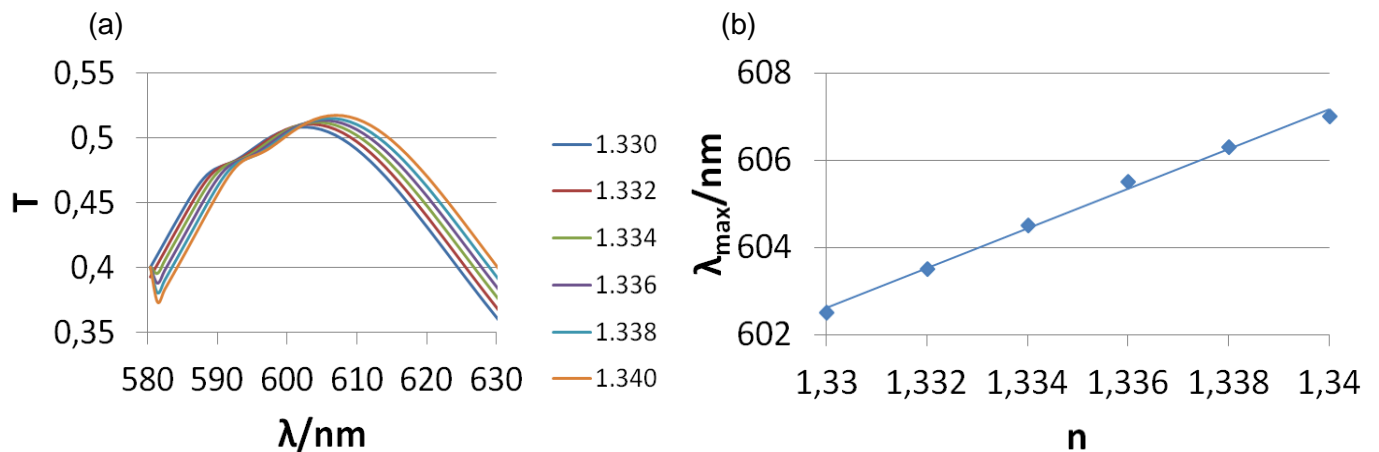


Figure 10.25: (a) Transmission spectra for different buffer refractive indexes, (b) sensitivity.

The sensitivity obtained for this structure is 455.71nm/RIU, this result is very similar to the obtained for the case in which the thickness of the gold film was 60nm. Furthermore, the transmission values are greater than in the case of working with thickness of 60nm.

Concerning to the near field maps, it is observed that the enhancement of the electric field in the Fabry-Perot resonance is smaller than in the wavelengths where resonances of EOT appear in the spectrum. This behavior is due to the enhancement is produced by the interaction between surface plasmons at both metal-dielectric interfaces. The Figure 10.26 illustrates this situation.

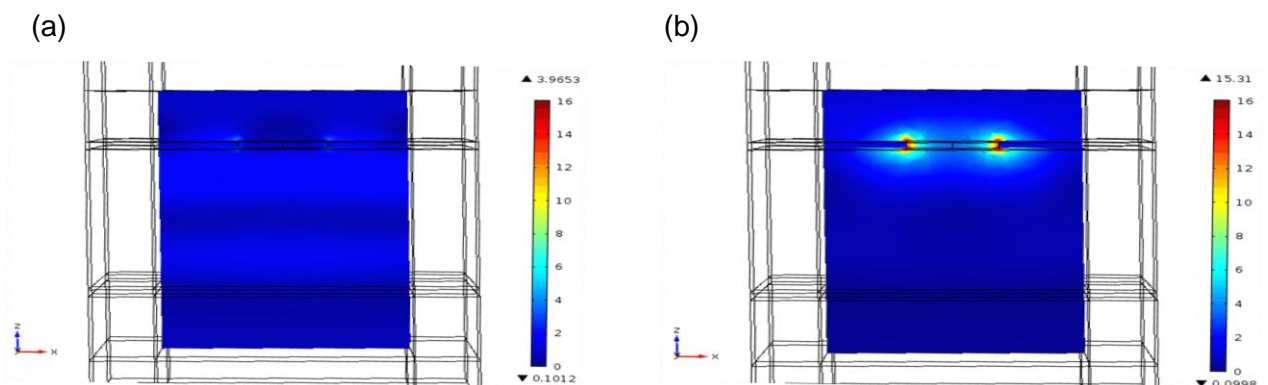


Figure 10.26: Near field images for the wavelengths where (a) Fabry-Perot (602nm) and (b) EOT resonances (760nm) are observed in spectrum.

Comparing the Figures 10.21 and 10.24, it is corroborated as the ratio  $t/D$ , being  $t$  the thickness film and  $D$  the nanoholes diameter, determines the width peaks. As  $t/D$  tends to unit, width decreases. For the last considered configuration (thickness of the gold film: 20nm). In this sense, the FWHM is double that in the case where thickness of the commented layer is 60nm.

We have proved that introducing a Fabry-Perot nanocavity increases biosensor sensitivity. However, the FWHM of the Fabry-Perot resonances is greater than the observed for the EOT peaks, which is a not desirable effect. For solving this drawback, we have increased nanocavity size, (as greater the nanocavity size is, smaller is the

FWHM, see the Figure 10.27). The microcavity size has been chosen for matching the EOT and Fabry-Perot resonances, increasing by this way sensitivity. In order to achieve this goal, we have considered a cavity with size 1140nm, Figure 10.28.

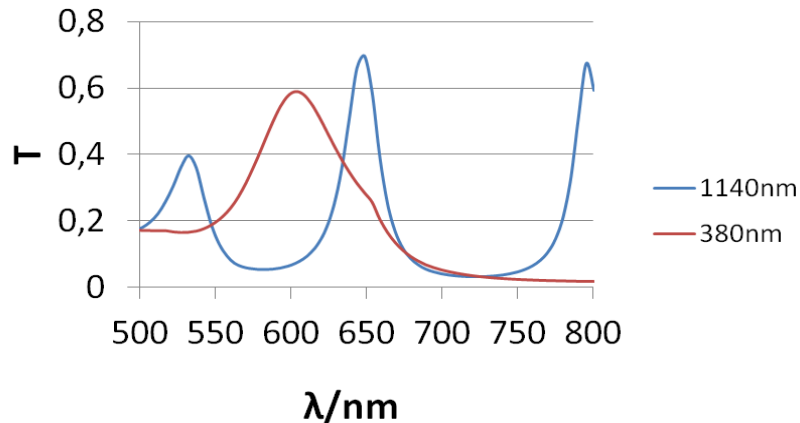


Figure 10.27: Transmission spectra for two different sizes of Fabry-Perot nanocavities.

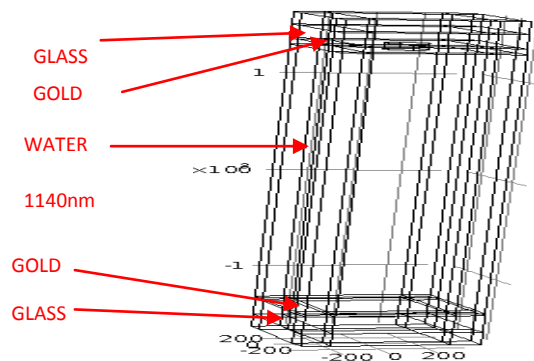


Figure 10.28: Scheme of the biosensor designed for matching the EOT and Fabry-Perot resonances.

Using this cavity, we are able to observe the Fabry-Perot resonance to 760nm, wavelength where the most intense EOT peak is observed in the basic configuration, shown in the Figure 10.9. For this situation, sensitivity is really high as it can be seen in Figure 10.29.

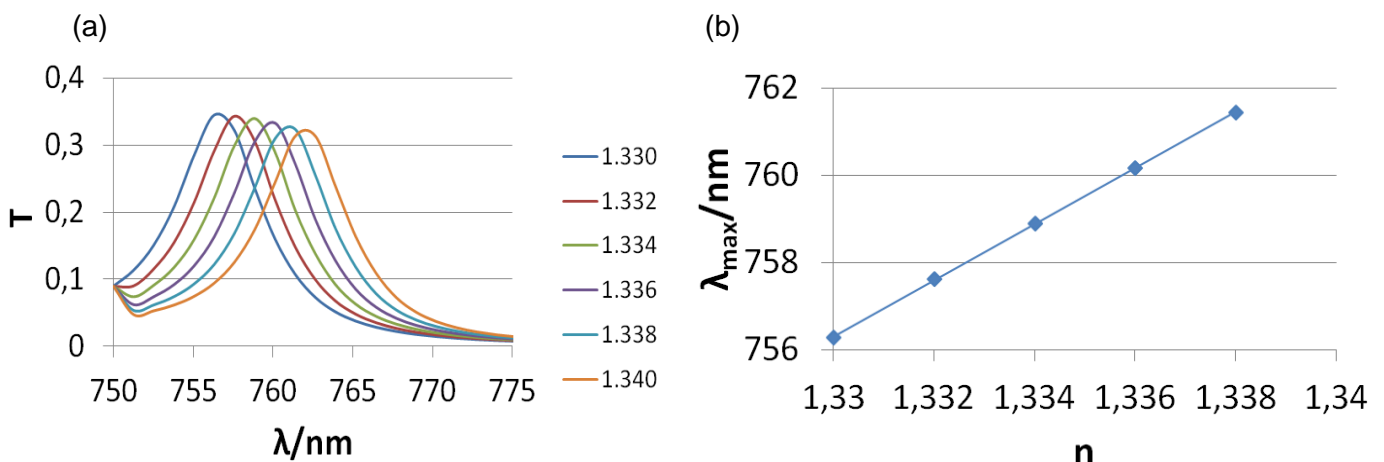


Figure 10.29: (a) Transmission spectra for different buffer refractive indexes, (b) sensitivity.

From Figures 10.29 (a) and (b) it is observed as the resonance peak is very sensible to small changes in the refractive index, concretely, the sensitivity obtained is: 642.5nm/RIU. Another remarkable fact is that peaks are very narrow.

When matching between both resonances is not as perfect as in the previous case, sensitivity decreases as it can be proved by the following Figure, 10.30.

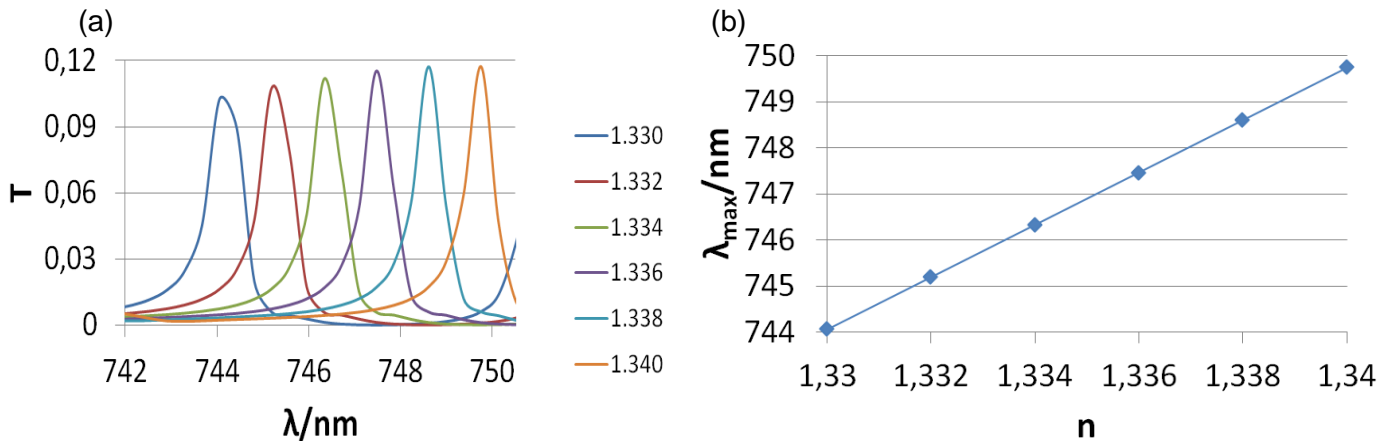


Figure 10.30: (a) Transmission spectra for different buffer refractive indexes, (b) sensitivity.

As can be seen, the sensitivity corresponding to 568.4nm/RIU, which is approximately 80nm/RIU lower than when matching between the EOT and Fabry-Perot resonances is better.

Through the results, it has been proved that designing a device where the sample is introduced in a Fabry-Perot nanocavity, the sensitivity increases. However, this configuration presents a disadvantage: the FWHM of the Fabry-Perot resonances is greater than the corresponding to the EOT peaks. Building a nanocavity of a determined size, generally around microns, it is possible to find Fabry-Perot resonances to the same wavelength as the EOT peaks, which supposes two different advantages: the FWHM of peaks decreases and sensitivity grows, reaching values as high as 650nm/RIU.

The only problem that presents the device described before is its difficulty of manufacturing, due to the necessary microfluidic for introducing the liquid buffer in the nanocavity. In fact, from an experimental point of view, the most practical configuration is observed in the Figure 10.14, where instead of the transmitted light, the reflected light would be analyzed. Some of its benefits are: peaks are narrower; ease of detecting minima; the sample is set on the nanohole array. However, the sensitivity of this configuration is a little bit low. So that, depending on the material to detect, it is necessary to get a balanced situation between sensitivity that you need and the manufacturing difficulty.

It has been carried out a study of the Extraordinary Optical Transmission phenomenon through subwavelength apertures perforated in metallic thin films. We have explored different nanostructures with the objective of increasing sensitivity, paying attention to a concrete design, which consists of a Fabry-Perot nanocavity where buffer is introduced. Due to amount of different variables that changes the behavior of this kind of devices: period, nanoholes diameter, metal...we decided to fix all of these parameters to 500, 180nm respectively and use gold as thin film. Before simulating biosensors, we have modelized the real problem in 2-D, where an object with a refractive index slightly higher than the corresponding to the buffer was immersed in it, for proving that the effective medium theory works well in our problem. Through the obtained results we extracted the following conclusions:

2-D simulations:

- The behavior of immersions with a refractive index of 1.40 in a liquid buffer whose refractive index is 1.33, and occupying a 3% of the total area, can be modeled by changes of 0.002 in the buffer refractive index, which allows us simulating this kind of devices in 3-D using the effective medium theory. The sensitivity results obtained using this theory will be a lower bound.

3-D simulations:

- Introducing a Fabry-Perot nanocavity, it is possible to observe Fabry-Perot resonances in the spectrum. If the gold layer, which constitutes the second nanocavity mirror, is about hundreds of nanometers, only reflection spectrum can be observed, due to gold absorption. In this case, the sensitivity is not as high as in another studied configurations but it presents two important advantages: detecting minima is easier than maxima and peaks are narrower. Also, it is easy of manufacturing.
- In the case where the second mirror of the Fabry-Perot nanocavity is thin, around 20nm, the transmission spectrum can be analyzed. By this way, it is observed that: if sample is set on the nanohole array, Fabry-Perot resonance is not sensible to changes in the buffer refractive index. So, it is necessary to introduce the buffer in the nanocavity. In this case, sensitivity reaches values as high as 490nm/RIU. The only problem of this configuration is the difficulty of manufacturing.
- Changing the thickness of thin films, transmission varies considerably. As thickness is lower, transmission is greater, due to the absorption in the metal film is not as high. Also, we corroborated the relation between the ratio  $t/D$  (thickness of metal film/nanoholes diameter) and the FWHM peaks. As  $t/D$  tends to unit, the FWHM decreases.
- Increasing the Fabry-Perot cavity width, we have matched the Fabry-Perot and EOT resonances, finding high sensitivities, corresponding to 650nm/RIU, and narrower peaks.

By this discussion, it is observed as designing a biosensor requires knowing its application previously in order to achieve the specified sensitivity but complicating as least as possible the manufacturing of the nanostructure used as biosensor.

### **Future work**

Concerning to future work, we show some projects that could be carried out, taking into account the amount of different parameters that play an important role in the biosensors sensitivity.

In the studied geometries, period should be changed. Sensitivity increases as this parameter does it too. In fact, we made some proofs during the development of this project, which consisted on changing the period to 700nm. We proved as sensitivity increased almost 200nm/RIU.

Another two parameters to change are the nanohole diameter and the metal film thickness, although it would be convenient do it by separate, in order to observe the effect of each one of them, [\[35\]](#).

Silver is another promising material in biosensors due to good optical response in visible range.

Apart from theoretical results, it would be important carry out experimental measurements, in order to compare both results. In fact, using a microscopy connected to a spectrometer, we have obtained experimentally transmission spectra of two nanoholes arrays, which have been provided by an external company. According between theoretical and experimental results was really good. Although, it would be necessary to manufacture the proposed biosensors in this project and, for a concrete buffer, study their sensitivity, which we think will be lower than the obtained theoretically.

## Bibliography

- [1] S. G. Rodrigo. *Study of the optical properties of nano-structured metallic systems with the Finite Difference Time Domain method*. Ph. D Thesis Universidad de Zaragoza, 2009.
- [2] H.F. Ghaemi, T. Thio, D.E. Grupp, T.W. Ebbesen, H.J. Lezec. Surface plasmons enhance optical transmission through subwavelength holes. *Physical Review B*, **58** (11), 1998.
- [3] T. Thio, H.J. Lezec, T.W. Ebbesen, K.M. Pellerin, G.D. Lewen, A. Nahata, R.A. Linke. Giant optical transmission of sub-wavelength apertures: physics and applications. *Nanotechnology*, **13**, 2002.
- [4] S. Carretero Palacios. *Mechanims for enhancing the optical transmission through a single subwavelength hole*. Ph. D Thesis Universidad de Zaragoza, 2011.
- [5] Heinz Raether. *Surface Plasmons on Smmoth and Rough Surfaces and on Gratings*. Springer-Verlag Berlin Heidelberg New York, 1988.
- [6] J. Casa Peláez. *Óptica*, Zaragoza: Cátedra de Óptica, Universidad, 1980. 4º Ed.
- [7] <http://www.bionavis.com/technology/spr/>
- [8] M. Couture, L.S. Live, A. Dhawan, J.-F. Masson. EOT or Kretschmann configuration? Comparative study of the plasmonic modes in gold nanohole arrays. *The Analyst*, **137**, 2012.
- [9] A.A. Yanik, A.E. Cetin, M. Huang, A. Artar, S. H. Mousavi, A. Khanikaev, J.H. Connor, et al. Seeing protein monolayers with naked eye through plasmonic Fano resonances. *Proceedings of the National Academy of Sciences of the United States of America*, **108**(29), 2011.
- [10] S. Ganci. Boundary diffraction wave theory for rectilinear apertures, *Eur.J.Phys*, 1997.
- [11] R. Gordon, D. Sinton, K.L. Kavanagh, & A.G. Brolo. A New Generation of Sensors Based on Extraordinary Optical Transmission, **41**(8), 2008.
- [12] L. Brigo, E. Gazzola, M. Cittadini, P. Zilio, G. Zacco, F. Romanato, A. Martucci, M. Guglielmi, G. Brusatin. Short and long range surface plasmon polariton waveguides for xylene sensing. *Nanotechnology*, **24**, 2013.
- [13] G. Parisi, P. Zilio, F. Romanato. Complex Bloch-modes calculation of plasmonic crystal slabs by means of finite elements method, *Optics Express*, **20**(15), 2012.
- [14] V. Giannini, Y. Zhang, M. Forcales, J. Gómez Rivas. Long-range surface polaritons in ultra-thin films of silicon. *Optics Express*, **16**(24), 2008.
- [15] E.D. Palik. *Handbook of Optical Constants of Solids*. Academic Press, New York, 1998.
- [16] G.A. Cervantes Tellez, S.Hassan, R.N. Tait, P. Berini, R.Gordon. Atomically flat symmetric elliptical nanohole arrays in a gold film for ultrasensitive refractive index sensing. *Lab on a chip*, **13**, 2013
- [17] R. Gordon, A.G. Brolo. Increased cut-off wavelength for a subwavelength hole in a real metal, *Optics Express*, **13**(6), 2005.
- [18] R. Ameling, L. Langguth, M. Hentschel, M. Mesch, P.V. Braun, H. Giessen. Cavity-enhanced localized plasmon resonance sensing. *Applied Physics Letters*, **97**, 2010.
- [19] J. Xu, P. Guan, P. Kvasni, H. Gong, Q. Yu. Light Transmission and Surface-Enhanced Raman Scattering of Quasi-3D Plasmonic Nanostructure Arrays with Deep and Shallow Fabry-Perot Nanocavities, *The journal of Physical Chemistry C*, **115**, 2011.
- [20] S.M. Jang, D. Kim, S.H. Choi, K.M. Byun, S.J. Kim. Enhancement of localized surface plasmon resonance detection by incorporating metal-dielectric double-layered subwavelength gratings. *Applied optics*, **50**(18), 2011.
- [21] N. Djaker, R. Hostein, E. Devaux, T.W. Ebbesen, H. Rigneault, J. Wenger. Surface Enhanced Raman Scattering on a Single Nanometric Aperture. *The Journal of Physical Chemistry C*, **114**(39), 2010.

- [22] L. Martín-Moreno, F. García-Vidal, H. Lezec, A. Degiron, T. Ebbesen. Theory of Highly Directional Emission from a Single Subwavelength Aperture Surrounded by Surface Corrugations. *Physical Review Letters*, **90**(16), 2003.
- [23] X. Gao, J.H. Shi, H.F. M.X. Jiang, T.J. Cui. Dual-band spoof surface plasmon polaritons based on composite-periodic gratings. *Journal of Physics D: Applied Physics*, **45**, 2012.
- [24] E. Hecht. *Óptica*. Madrid: Addison-Wesley Iberoamericana, D.L. 1999. 3º Ed.
- [25] D. Maystre. *Theory of Wood's Anomalies*. Springer-Verlag Berlin Heidelberg New York, 2012.
- [26] A. Hessel, A.A. Oliner. A New Theory of Wood's Anomalies on Optical Gratings. *Applied Optics*, **4**(10), 1965.
- [27] J.M. McMahon, J. Henzie, T.W. Odom, G.C. Schatz, S.K. Gray. Tailoring the sensing capabilities of nanohole arrays in gold films with Rayleigh anomaly-surface plasmon polaritons. *Optics Express*, **15**(26), 2007.
- [28] T.-W. Lee, S.K. Gray. *Subwavelength light bending by metal slit structures*. *Optics Express*, **13**(24), 2005.
- [29] C. F. Bohren, D. R. Huffman, *Absorption and Scattering of Light by Small Particles*, John Wiley & Sons, 1983.
- [30] A. Barreda Gómez. Electromagnetic behavior of nanoparticle dimmers. Proyecto Fin Grado, 2013.
- [31] T.I. Wong, S. Han, L. Wu, Y. Wang, J. Deng, C.Y.L. Tan, P. Bai, et al. High throughput and high yield nanofabrication of precisely designed gold nanohole arrays for fluorescence enhanced detection of biomarkers. *Lab on a chip*, DOI: 10.1039/c3lc41396a.
- [32] X. Heng, X. Cui, D.W. Knapp, J. Wu, Z. Yaqoob, E. J. McDowell, D. Psaltis, et al. Characterization of light collection through a subwavelength aperture from a point source. *Optics Express*, **14**(22), 2006.
- [33] W.J. Choi, D.I. Jeon, S.-G. Ahn, J.-H. Yoon, S. Kim, B. H. Lee. Full-field optical coherence microscopy for identifying live cancer cells by quantitative measurement of refractive index distribution. *Optics Express*, **18**(22), 2010.
- [34] R. Gordon, A.G. Brolo, D. Sinton, K.L. Kavanagh. Resonant Optical Transmission through hole-arrays in metal films: physics and applications. WILEY-VCH Verlag GmbH & Co. KGaA, Weinheim, 2009.
- [35] J.S. Kee, S. Lim, A.P. Perera, M.K. Park, Y. Zhang. Plasmonic nanohole array for biosensor applications. *Photonics Global Conference (PGC)*, 2012.

### **List of Figures:**

- Figure 1.1 (a): J. Zhang, L. Zhang, W. Xu. (2012). Surface plasmon polaritons: physics and applications. *Journal of Physics D: Applied Physics*, **45**, 2012.
- Figure 1.1 (b): <http://theses.ulaval.ca/archimede/fichiers/24879/ch05.html>
- Figure 1.8: <http://www.bionavis.com/technology/spr/>
- Figure 1.10: <http://www.photonics.com/Article.aspx?AID=23952>
- Figure 4.6 (a): [\[18\]](#)
- Figure 4.6 (b): [\[19\]](#)
- Figure 4.6 (c): [\[20\]](#)
- Figure 4.6 (d): [\[23\]](#)
- Figure 5.1: <http://nanolithography.spiedigitallibrary.org/article.aspx?articleid=1098659>